Geosci. Model Dev. Discuss., doi:10.5194/gmd-2016-271, 2016
Manuscript under review for journal Geosci. Model Dev.
Published: 28 November 2016

Geoscientific Model Development Discussions
Open Access
EGU

Collection/aggregation algorithms in Lagrangian cloud microphysical models: Rigorous evaluation in box model simulations

Simon Unterstrasser[1], Fabian Hoffmann[2], and Marion Lerch[1]

[1]Deutsches Zentrum für Luft- und Raumfahrt (DLR) – Institut für Physik der Atmosphäre, Oberpfaffenhofen, 82234 Wessling, Germany.
[2]Leibniz Universität Hannover – Institute of Meteorology and Climatology, 30419 Hannover, Germany.

Correspondence to: Simon Unterstrasser: simon.unterstrasser@dlr.de

Abstract. Recently, several Lagrangian microphysical models have been developed which use a large number of (computational) particles to represent a cloud. In particular, the collision process leading to coalescence of cloud droplets or aggregation of ice crystals is implemented differently in the various models. Three existing implementations are reviewed and extended, and their performance is evaluated by a comparison with well established analytical and bin model solutions. In this first step of rigorous evaluation, box model simulations with collection/aggregation being the only process considered have been performed for the three well-known kernels of Golovin, Long and Hall.

Besides numerical parameters like the time step and the number of simulation particles (SIPs) used, the details of how the initial SIP ensemble is created from a prescribed analytically defined size distribution is crucial for the performance of the algorithms. Using a constant weight technique as done in previous studies greatly underestimates the quality of the algorithms. Using better initialisation techniques considerably reduces the number of required SIPs to obtain realistic results. From the box model results recommendations for the collection/aggregation implementation in higher dimensional model setups are derived. Suitable algorithms are equally relevant to treating the warm-rain process and aggregation in cirrus.

1 Introduction

The collection of cloud droplets or the aggregation of ice crystals is an important process in liquid and ice clouds. By changing the size, number, and in the case of ice the shape of hydrometeors, collection and aggregation affect the microphysical behaviour of clouds and thereby their role in the climate system.

The warm rain process (i.e. the production of precipitation in clouds in the absence of ice) depends essentially on the collision and subsequent coalescence of cloud droplets. At its initial stage,

Geosci. Model Dev. Discuss., doi:10.5194/gmd-2016-271, 2016
Manuscript under review for journal Geosci. Model Dev.
Published: 28 November 2016

Geoscientific Model Development Discussions
Open Access
EGU

however, condensational growth governs the activation of aerosols and the following growth of cloud droplets, which might initiate the collection process if they become sufficiently large. Then, collection produces drizzle or raindrops, which are able to precipitate from the cloud, affecting lifetime and organisation of clouds (e.g. Albrecht, 1989; Xue et al., 2008).

In ice clouds, sedimentation, deposition growth and in particular radiative properties depend on the ice crystals' habits (Sölch and Kärcher, 2011, and references therein). Ice aggregates scatter more strongly shortwave radiation than pure ice crystals of the same mass. Recent simulation results suggest that contrail-cirrus and natural cirrus can be strongly interwoven. In the mixing area with ice crystals of both origins being present, a prominent bimodal spectrum occurs and enhances the probability of collisions (Unterstrasser et al., 2016).

The temporal change of the droplet number distribution by the collision and subsequent coalescence of droplets (or any other particles) is described by the stochastic collection equation (SCE), also known as kinetic collection equation, coagulation equation, Smoluchowksi or population balance equation (e.g. Wang et al., 2007). It yields:

$$\frac{\partial f_m(m,t)}{\partial t} = \frac{1}{2}\int_0^m K(m',m-m')f_m(m',t)f_m(m-m',t)\,dm' - \int_0^\infty K(m,m')f_m(m,t)f_m(m',t)\,dm', \tag{1}$$

where $f_m(m)dm$ is the number concentration within an infinitesimal interval around the mass m. The first term (gain term) accounts for the coalescence of two smaller droplets forming a new droplet with mass m, the second term (loss term) accounts for the coalescence of m-droplets with any other droplets forming a larger droplet. The collection kernel $K(m,m')$ describes the rate by which a m-droplet-m'-droplet-collection occurs. Due to the symmetry of the collection kernel ($K(m,m') = K(m',m)$) the first term of the right-hand side can also be written as $\int_0^{m/2} K(m',m-m')f_m(m',t)f_m(m-m',t)\,dm'$.

For several kernel functions (mostly of polynomial form) analytic solutions exist for specific initial distributions (Golovin, 1963; Berry, 1967; Scott, 1968). The Golovin kernel (sum of masses) is given by

$$K(m,m') = b\,(m+m'). \tag{2}$$

Solutions for more realistic kernels (Long, 1974; Hall, 1980; Wang et al., 2006) and arbitrary initial distribution can be obtained with various numerical methods mainly using a bin representation of the droplet size distribution (Berry and Reinhardt, 1974; Tzivion et al., 1987; Bott, 1998; Simmel et al., 2002; Wang et al., 2007). The hydrodynamic kernel is defined as

$$K(r,r') = \pi(r+r')^2\,|w_{sed}(r) - w_{sed}(r')|\,E_c(r,r'), \tag{3}$$

Geosci. Model Dev. Discuss., doi:10.5194/gmd-2016-271, 2016
Manuscript under review for journal Geosci. Model Dev.
Published: 28 November 2016

Geoscientific Model Development Discussions
Open Access
EGU

based on the radius r and the sedimentation velocity w_{sed}. Parametrisations of the collection efficiency E_c are given, e.g. by Long (1974) or Hall (1980). In the above formula, the differential sedimentation is the driver of collections. No same-size collisions can occur, i.e. $K(r,r) = 0$. More sophisticated expressions for $K(r,r')$ have been derived to include turbulence enhancement of the collisional growth, which also allow same-size collisions ($K(r,r) > 0$) (e.g. Ayala et al., 2008; Grabowski and Wang, 2013; Chen et al., 2016).

Solving (1) demands simplifications in the representation of the droplet spectrum for which several numerical models have been developed. Spectral-bin models (e.g. Khain et al., 2000) represent the spectrum by dividing it into several intervals, so-called bins. This approach enables the prediction of the temporal development of the droplet number concentration in each bin by using finite differences or more sophisticated numerical techniques (e.g. Bott, 1998). The accuracy of these models is primarily determined by the number of used bins (usually on the order of 100), which makes them computationally challenging and prohibits their use in day-to-day applications like numerical weather prediction. Less challenging but less accurate, cloud microphysical bulk models compute the temporal change of integral quantities of the droplet spectrum (e.g. Kessler, 1969; Khairoutdinov and Kogan, 2000; Seifert and Beheng, 2001). These are usually equations for the temporal evolution of bulk mass (so-called one-moment schemes), and additionally number concentration (two-moment schemes) or radar reflectivity (three-moment schemes), which describe the change of the entities of cloud droplets and rain drops (in the case of warm clouds). The separation radius between cloud droplets and rain drops depends on the details of the bulk scheme, but generally cloud droplets (up to 20 to 40 μm in radius) are assumed to have negligible sedimentation fall velocities, while larger drops, frequently subsumed as rain drops, have significant sedimentation velocities to cause collision/coalescence. The interactions of cloud and rain drops are therefore described in terms of self-collection (coalescence of cloud (rain) drops resulting in cloud (rain) drops), autoconversion (coalescence of cloud droplets resulting in rain drops) and accretion (collection of cloud droplets by rain drops). A third alternative for computing cloud microphysics has been developed in the recent years: Lagrangian cloud models (LCMs). These models represent cloud microphysics on the basis of individual particles. Similar to spectral-bin models, LCMs enable the detailed representation of droplet spectra but inherently avoid spurious numerical diffusion in condensational and collisional growth usually affecting the results of spectral-bin models (Andrejczuk et al., 2010; Arabas and Shima, 2013).

To our knowledge, five fully coupled LCMs for warm clouds exist, which are described in Andrejczuk et al. (2008); Shima et al. (2009); Riechelmann et al. (2012); Arabas et al. (2015) and Naumann and Seifert (2015) and have been extended or applied in various problems (e.g. Andrejczuk et al., 2010; Arabas and Shima, 2013; Lee et al., 2014; Hoffmann et al., 2015). For ice clouds, three models exist (Paoli et al., 2004; Shirgaonkar and Lele, 2006; Sölch and Kärcher, 2010) which have been applied to natural cirrus (Sölch and Kärcher, 2011) and, in particular, to contrails (e. g. Paoli et al., 2013; Unterstrasser, 2014;

Geosci. Model Dev. Discuss., doi:10.5194/gmd-2016-271, 2016
Manuscript under review for journal Geosci. Model Dev.
Published: 28 November 2016

Geoscientific Model Development Discussions
Open Access
EGU

Unterstrasser and Görsch, 2014). In the context of ice clouds and warm clouds, different names are used for processes that are similar, in particular in terms of their numerical treatment (deposition/sublimation vs. condensation/evaporation, collection vs. aggregation). Conceptually similar are particle based approaches in aerosol physics (Riemer et al., 2009; Maisels et al., 2004) which account for coagulation of aerosols (DeVille et al., 2011; Kolodko and Sabelfeld, 2003).

So far, no consistent terminology has been used in the latter publications. Various names have been used for the same things by various authors. We point out that super droplet, computational droplet and simulation particle (SIP) all have the same meaning and refer to a bunch of identical real cloud droplets (or ice crystals). The number of real droplets represented in a SIP is denoted as weighting factor or multiplicity. Moreover, Lagrangian approaches in cloud physics have been named Lagrangian Cloud Model (LCM), super droplet method (SDM) or particle based method. In this paper, we use the terms SIP, weighting factor ν_{sim} and LCM. Here droplet refers to either real droplets or ice crystals.

Usually, only the liquid water or the ice of a cloud are described with a Lagrangian representation, whereas all other physical quantities (like velocity, temperature and water vapour concentration) are described in Eulerian space (see also discussion in Hoffmann, 2016). SIPs have discrete positions $\mathbf{x}_p = (x_p, y_p, z_p)$ within a grid box. The position is regularly updated obeying the transport equation $\partial \mathbf{x}_p / \partial t = \mathbf{u}$. Microphysical processes like sedimentation and droplet growth are treated individually for each SIP. Interpolation methods can be used to evaluate the Eulerian fields at the specific SIP positions. This implicitly assumes that all ν_{sim} droplets of the SIPs are located at the same position. On the other hand, the droplets of a SIP are assumed to be well-mixed in the grid box in LCM treatment of collection and sometimes condensation. Then, the number concentration represented by a single SIP, e. g., is given by $\nu_{sim}/\Delta V$, where ΔV is the volume of the grid box.

Lists of used symbols and abbreviation are given in Tables 1 and 2.

2 Description of the various collection/aggregation implementations

We use the terminology of Berry (1967), where $f_{\ln r}$ and $g_{\ln r}$ denote the number and mass density function with respect to the logarithm of droplet radius $\ln r$. The relations $g_{\ln r}(r) = m f_{\ln r}(r)$ and $f_{\ln r}(r) = 3 m f_m(m)$ hold. The latter designates the number density function with respect to mass and obeys the transformation property of distributions: $f_y(y)dy = f_x(x(y))dx$. For consistency with previous studies, $g_{\ln r}$ is used for plotting purposes, whereas f_m and g_m are more relevant in the following analytical derivations.

The moments of order k of the mass distribution f_m (= number density function with respect to mass) are defined as:

$$\lambda_k(t) = \int m^k f_m(m,t) dm. \tag{4}$$

Geosci. Model Dev. Discuss., doi:10.5194/gmd-2016-271, 2016
Manuscript under review for journal Geosci. Model Dev.
Published: 28 November 2016

Geoscientific Model Development Discussions
Open Access
EGU

Table 1. List of symbols.

Symbol	Value/Unit	Meaning
$f_m, \tilde{f}_m$	$\mathrm{kg}^{-1}\ \mathrm{m}^{-3}$, 1	(normalised) droplet number concentration per mass interval
$g_m, g_{\ln r}$	m^{-3}, $\mathrm{kg\ m}^{-3}$	droplet mass concentration per mass interval/per logarithmic radius interval
$m,\ m'$	kg	mass of a single real droplet
m_{bb}	kg	bin boundaries of the bin grid
$\bar{m} = \lambda_1/\lambda_0 = \mathcal{N}/\mathcal{M}$	kg	mean mass of all droplets
$n_{bin,l}$	1	droplet number in bin l
$r,\ r'$	m	droplet radius
r_{lb}	m	threshold radius in $\nu_{random,lb}$-init
$r_{critmin}$	m	lower cut-off radius in singleSIP-init
w_{sed}	$\mathrm{m\,s}^{-1}$	sedimentation velocity
$DNC = \lambda_0$	m^{-3}	droplet number concentration
E_c	1	collection/aggregation efficiency
K	$\mathrm{m}^3\ \mathrm{s}^{-1}$	collection/aggregation kernel
$LWC = \lambda_1$	$\mathrm{kg\,m}^{-3}$	droplet mass concentration, liquid water content
$M_{bin,l}$	kg	total droplet mass in bin l
N_{SIP}	1	number of SIPs
N_{BIN}	1	number of bins
$\alpha_{low}, \alpha_{med}, \alpha_{high}$	1	parameters of the ν_{random}-init method.
Δt	s	time step
ΔV	m^3	grid box volume
η	1	parameter in RMA algorithm and singleSIP-init method
κ	1	number of bins per mass decade
λ_k	$\mathrm{kg}^k\ \mathrm{m}^{-3}$	moments of the order k
μ	kg	single droplet mass of a SIP
$\nu_{critmax}$	1	maximum number of droplets represented by a SIP
$\nu_{critmin}$	1	minimum number of droplets represented by a SIP
ν	1	number of droplets represented by a SIP
ξ	1	splitting parameter of AON algorithm
$\chi = \mu\,\nu,\ \tilde{\chi} = \chi/\mathcal{M}$	kg, 1	total droplet mass of a SIP
$\mathcal{N} = \lambda_0 \Delta V$	1	total droplet number
$\mathcal{M} = \lambda_1 \Delta V$	kg	total droplet mass
$\mathcal{Z} = \lambda_2\,\Delta V$	kg^2	second moment of droplet mass distribution (radar reflectivity)

Geosci. Model Dev. Discuss., doi:10.5194/gmd-2016-271, 2016
Manuscript under review for journal Geosci. Model Dev.
Published: 28 November 2016

Geoscientific Model Development Discussions
Open Access
EGU

Table 2. List of abbreviations.

AON	All-Or-Nothing algorithm	AIM	Average Impact algorithm
DSD	droplet size distribution	LCM	Lagrangian Cloud Model
PDF	probability density function	RMA	Remapping algorithm
SIP	simulation particle		

The low order moments represent the number concentration ($DNC = \lambda_0$) and the mass concentration ($LWC = \lambda_1$). The analogous extensive properties $\lambda_k(t)\,\Delta V$ are the total droplet number $\mathcal{N}$, total droplet mass $\mathcal{M}$ and radar reflectivity ($\mathcal{Z} = \lambda_2\,\Delta V$). For a given SIP ensemble, the moments can be simply computed by

$$\lambda_{k,SIP}(t) = \left(\sum_{i=0}^{N_{SIP}} \nu_i {\mu_i}^k \right) / \Delta V, \tag{5}$$

where μ_i is the single droplet mass of SIP i and N_{SIP} is the number of SIPs inside a grid box. For reasons of consistency with Wang et al. (2007), we translate the SIP ensemble into a mass distribution g_m in bin representation and then compute the moments with the formula

$$\lambda_{k,BIN}(t) = \sum_{i=0}^{N_{BIN}} g_m(m_i,t)(\tilde{m}_{bb,l})^{k-1} \frac{\ln 10}{3\,\kappa} \tag{6}$$

(cf. with their equation 48).

The initialisation is successful for a given parameter set, if the moments of the SIP ensemble $\lambda_{k,SIP}$ are close to the analytical values $\lambda_{k,anal}$. For an exponential distribution (as used in this study), the probability density function (PDF) reads as

$$f_m(m) = \frac{\mathcal{N}}{\Delta V \bar{m}} \exp\left(-\frac{m}{\bar{m}}\right), \tag{7}$$

the moments are given analytically by

$$\lambda_{k,anal}(t) = (k-1)!\,\mathcal{N}\,\bar{m}^k/\Delta V, \tag{8}$$

where $k!$ is the faculty of k and $\bar{m} = \mathcal{M}/\mathcal{N}$ the mean mass (Rade and Westergren, 2000).

Throughout this study, the initial parameters of the droplet size distribution (DSD) are $DNC_0 = 2.97 \times 10^8$ m^{-3} and $LWC_0 = 10^{-3}$ kg m^{-3} (implying a mean radius of 9.3 μm) as in Wang et al. (2007). The higher moments are $\lambda_{2,anal} = 6.74{\times}10^{-15}$ kg^{2}m^{-3} and $\lambda_{3,anal} = 6.81{\times}10^{-26}$ kg^{3}m^{-3}.

2.1 Initialisation

In our test cases, all microphysical processes except collection are neglected and an exponential DSD is initialised. In the results section, we will demonstrate that the outcome of the various collection algorithms critically depends on how this initial, analytically defined, continuous DSD is translated into a discrete ensemble of SIPs. Hence, the SIP initialisation is described in some detail.

Geosci. Model Dev. Discuss., doi:10.5194/gmd-2016-271, 2016
Manuscript under review for journal Geosci. Model Dev.
Published: 28 November 2016

Geoscientific Model Development Discussions
Open Access
EGU

2.1.1 SingleSIP-init and MultiSIP-init

First, the mass distribution is discretized on a logarithmic scale. The boundaries of bin l are given by $m_{bb,l} = m_{low} 10^{l/\kappa}$ and $m_{bb,l+1}$, where m_{low} is the minimum droplet mass considered. The bin centre is computed using the arithmetic mean $\bar{m}_{bb,l} = 0.5\,(m_{bb,l+1} + m_{bb,l})$. The bin size is $\Delta m_{bb,l} = (m_{bb,l+1} - m_{bb,l})$. The mass increases tenfold every κ bins. Several previous studies used the parameter s with $m_{bb,l+1}/m_{bb,l} = 2^{1/s}$ to characterise the bin resolution. The parameters s and κ are related via $s = \kappa \log_{10}(2) \approx 0.3\,\kappa$.

For each bin, the droplet number is approximated by $\nu_b = f_m(\bar{m}_{bb,l})\,\Delta m_{bb,l} \Delta V$ and one SIP with weighting factor $\nu_{sim} = \nu_b$ and droplet mass $\mu_{sim} = \bar{m}_{bb,l}$ is created, if ν_b is greater than a lower cut-off threshold $\nu_{critmin}$. No SIP is created, if $\nu_b < \nu_{critmin}$. Moreover, no SIPs are created from bins with radius $r < r_{critmin}$. We will refer to this as deterministic singleSIP-init. In its probabilistic version, the mass μ_{sim} is randomly chosen within each bin l and $\nu_{sim} = f_m(\mu_{sim})\,\Delta m_{bb,l} \Delta V$ is adapted accordingly. By default, $r_{critmin} = 0.6\,\mu\mathrm{m}$ and $\nu_{critmin} = \eta \times \nu_{max}$, which is determined from the maximal weighting factor within the entire SIP ensemble ν_{max} and the prescribed ratio of the minimal to the maximal weighting factor $\eta = 10^{-9}$. For larger $r_{critmin}$ it is advantageous to initialise one additional "residual" SIP that contains the sum of all neglected contributions.

Following Unterstrasser and Sölch (2014, see their Appendix A), we introduce the multiSIP-init technique. It is similar to singleSIP-init technique, except that we additionally introduce an upper threshold $\nu_{critmax}$. If $\nu_b > \nu_{critmax}$ is fulfilled for a specific bin, then this bin is divided into $\kappa_{sub} = \lceil \nu_b / \nu_{critmax} \rceil$ sub-bins and a SIP is created for each sub-bin. The multiSIP-init technique gives a good trade-off between resolving low concentrations at the DSD tails and high concentrations of the most abundant droplet masses.

So far, we introduced initialisation techniques with a strict lower threshold $\nu_{critmin}$ with no SIPs created in bins with $\nu_b < \nu_{critmin}$. We can relax this condition by introducing—what we call—a *weak* threshold. This means, that in such low contribution bin (with $\nu_b < \nu_{critmin}$) we create a SIP with the probability $p_{create} = \nu_b / \nu_{critmin}$ and weighting factor $\nu_{sim} = \nu_{critmin}$. Having many realisations of initial SIP ensembles, the expectation value of the droplet number represented by such SIPs, $\nu_{critmin} \cdot p_{create} + 0 \cdot (1 - p_{create})$, equals the analytically prescribed value ν_b. Using a strict threshold the droplet number would be simply 0 in those low contribution bins. In a related problem, such a probabilistic approach has been shown to strongly leverage the sensitivity of ice crystal nucleation on the numerical parameter $\nu_{critmin}$. This led to a substantial reduction of the number of SIPs that are required for converging simulation results (Unterstrasser and Sölch, 2014).

Using the probabilistic version and a weak lower threshold is particularly important if different realisations of SIP ensembles of the same analytic DSD should be created. The number of SIPs N_{SIP} depends on κ, $\nu_{critmin}, \nu_{critmax}$ and the parameters of the prescribed distribution.

Moreover, the singleSIP-init is used in a hybrid version, where different κ-values are used in specified radius ranges.

Geosci. Model Dev. Discuss., doi:10.5194/gmd-2016-271, 2016
Manuscript under review for journal Geosci. Model Dev.
Published: 28 November 2016

Geoscientific Model Development Discussions
Open Access
EGU

2.1.2 ν_{const}-init and ν_{draw}-init

The accumulated PDF $F(m)$ is given by $\int_0^m \tilde{f}_m(m')dm'$ with the normalised PDF $\tilde{f}_m = f_m/\lambda_0$. First, the size N_{SIP} of the SIP ensemble that should approximate the initial DSD is specified. For each SIP, its mass μ_i is reasonably picked by

$$\mu_i = F^{-1}(\text{rand}()),$$

where rand() generates uniformly distributed random numbers $\in [0,1]$. In case of the ν_{const}-init, the weighting factors of all SIPs are equally $\nu_i = \nu_{const} = \mathcal{N}/N_{SIP}$. This init method reproduces SIP ensembles similar to the ones in Shima et al. (2009) or Hoffmann et al. (2015). As a variety of the ν_{const}-init method, the weighting factors ν_i in the ν_{draw}-init method are simply perturbed by $\nu_i = 2\,\text{rand}()\,\nu_{const}$.

For the case of an exponential distribution, the following holds for the SIPs $i = 1, N_{SIP}$:

$$\mu_i = -\bar{m}\log(\text{rand}()).$$

In the literature, this approach is known as inverse transform sampling. A proof of correctness can be found in classical textbooks, e.g. Devroye (1986, their section II.2).

2.1.3 ν_{random}-init

The third approach allows specifing the spectrum of weighting factors that should be covered by the SIP ensemble. Similar to the ν_{draw}-init method, the weighting factors are randomly determined. Whereas the latter method produced a SIP ensemble with weighting factors uniformly distributed in ν, the ν_{random}-init produces weighting factors uniformly distributed in $\log(\nu)$ and covering the range $[\mathcal{N}\,10^{\alpha_{low}}, \mathcal{N}\,10^{\alpha_{high}}]$. The eventual number of SIPs depends most sensitively on the parameter α_{high}, which controls how big the portion of a single SIP can be.

SIPs with weighting factors $\nu_i = \mathcal{N}\,10^{(\alpha_{low}+(\alpha_{high}-\alpha_{low})\cdot\text{rand}())}$ are created, until $\sum_{j=1}^{N_{SIP}} \nu_j$ exceeds $\mathcal{N}$. The weighting factor of the last SIP is corrected such that $\sum_{j=1}^{N_{SIP}} \nu_j = \mathcal{N}$ holds. Now the mass μ_i of each SIP is determined by the following technique: The first SIP represents the smallest droplets and covers the mass interval $[0, m_1]$, whereas the last SIP represents the largest droplets in the interval $[m_{N_{SIP}-1}, \infty]$. The SIPs i in between cover the adjacent mass intervals $[m_{i-1}, m_i]$. The boundaries are implicitly determined by $\int_0^{m_i} f_m(m')dm'\,\Delta V = \sum_{j=1}^{i} \nu_j$. The total mass contained in each SIP is given by $\chi_i = \int_{m_{i-1}}^{m_i} f_m(m')m'dm'\,\Delta V$ and the single droplet mass by $\mu_i = \chi_i/\nu_i$.

For the case of an exponential distribution, the following holds for the interval boundaries and the SIPs $i = 1, N_{SIP}$:

$$m_i = -\bar{m}\log\left(\mathcal{N} - \sum_{j=0}^{i} \nu_j\right)$$

Geosci. Model Dev. Discuss., doi:10.5194/gmd-2016-271, 2016
Manuscript under review for journal Geosci. Model Dev.
Published: 28 November 2016

and

$$\mu_i = \left(\frac{m_{i-1} - \bar{m}}{\exp(m_{i-1}/\bar{m})} - \frac{m_i - \bar{m}}{\exp(m_i/\bar{m})} \right) \frac{\mathcal{N}}{\nu_i}.$$

The above formulas must be carefully implemented such that numerical cancellation errors are kept tolerable.

Experimenting with the SIP-init procedure, several optimisations have been incorporated. First, the ν-spectrum is split into two intervals $[\mathcal{N}\,10^{\alpha_{low}},\ \mathcal{N}\,10^{\alpha_{med}}]$ and $[\mathcal{N}\,10^{\alpha_{med}},\ \mathcal{N}\,10^{\alpha_{high}}]$. We alternately pick random values from the two intervals. Without this correction, it happened that several consecutive SIPs with small weights and hence nearly identical droplet masses are created, which increases the SIP number without any benefits.

Going through the list of SIPs, the droplet masses increase and hence the individual SIPs contain gradually increasing fractions of the total grid box mass. This can lead to a rather coarse representation of the right tail of the DSD. Two options to improve this have been implemented. In the $\nu_{random,rs}$-option, the ν_i-values are reduced by some factor, that increases, as $\sum_{j=1}^{i} \nu_j$ approaches $\mathcal{N}$. In the $\nu_{random,lb}$-option, ν-values are randomly picked up to a certain radius threshold r_{lb}. Above this threshold, SIPs are created with the singleSIP-method used on a linear bin.

2.1.4 Comparison

Figure 1 shows the weighting factors and other properties of the initial SIP ensemble, which may affect the performance of the algorithms. Each column shows one class of initialisation techniques. For a certain realisation, the first row shows the weighting factors ν_i of all SIPs as a function of their represented droplet radius r_i. Each dot shows the (ν_i, r_i)-pair of one SIP. For the singleSIP-init, the dots are uniformly distributed along the horizontal axis, as one SIP is created from each bin (with exponentially increasing bin sizes). The according ν-values relate directly to the prescribed DSD. The higher $f_m \Delta m$, the more droplets are represented in a SIP. No SIPs smaller than $r_{critmin} = 0.6\,\mu\mathrm{m}$ are initialised and the ν-values range over nine orders of magnitude consistent with $\eta = 10^{-9}$. The MultiSIP-init introduces an upper bound of $\nu_{critmax} = 2 \cdot 10^6$ for ν. This threshold is effective over a certain radius range where the SIPs have lower ν-values compared to the singleSIP-init and are also more densely distributed along the horizontal axis. For the ν_{const}-init, all SIPs use $\nu = \nu_{const}$, whereas for the ν_{draw}-init the ν-values scatter around this value. For ν_{const} and ν_{draw}, the ν-values are chosen independently of the given DSD contrary to the latter techniques. However, for both techniques, the density of the dots along the r-axis is correlated to $f_m \Delta m$.

The ν_{random}-init technique randomly picks ν-values which are distributed over a larger range compared to the ν_{draw}-init. In fact, they are uniformly distributed in $\log(\nu)$. The range of possible ν-values can be adjusted and is chosen similar to the singleSIP/multiSIP by setting $\alpha_{high} = -2, \alpha_{med} = -3$ and $\alpha_{low} = -7$. One possible advantage compared to the singleSIP-approach could be that the occurrence of certain ν-values is not limited to a certain radius range. In the singleSIP-

Geosci. Model Dev. Discuss., doi:10.5194/gmd-2016-271, 2016
Manuscript under review for journal Geosci. Model Dev.
Published: 28 November 2016

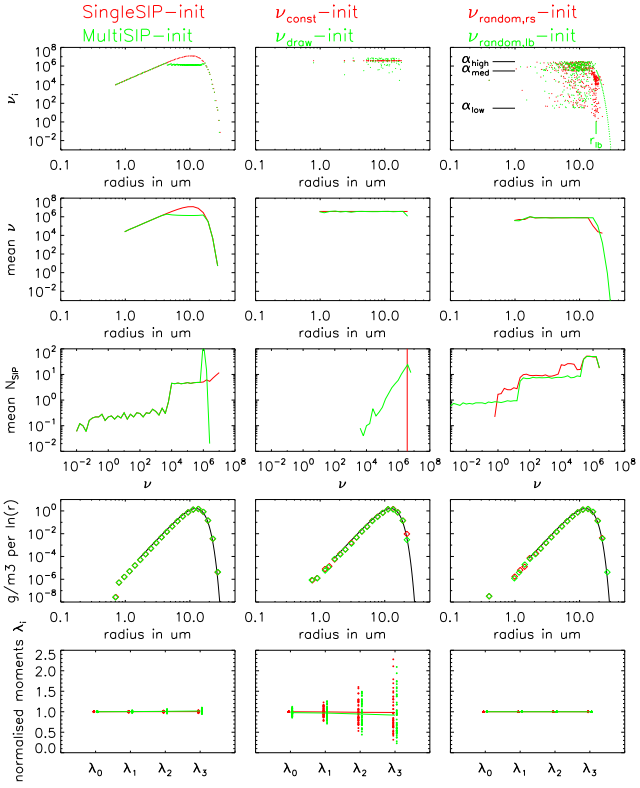

Figure 1. Characteristics of the various SIP initialisation methods (as given on top of each panel): Weighting factors $\nu_i(r_i)$ of an initial SIP ensemble, the mean weighting factors $\bar{\nu}(r)$, the occurrence frequency of the ν_i-values and the resulting mass density distributions $g_{\ln r}$are displayed (Row 1 to 4). Row 1 displays data of a single realisation, whereas rows 2 to 4 show averages over 50 SIP ensembles. The bottom row shows the moments λ_0, λ_1, λ_2 and λ_2 normalised by the respective analytical value. Every symbol depicts the value of a single realisation. The nearly horizontal line connects the mean values over all realisations. In the displayed examples, $\kappa = 20$ in the singleSIP-init, $\kappa = 20$, $\nu_{critmax} \approx 2 \cdot 10^6$ in the multiSIP-init, $N_{SIP} = 80$ in the ν_{const}, ν_{draw}-init and $(\alpha_{high}, \alpha_{med}, \alpha_{low}) = (10^{-2}, 10^{-3}, 10^{-7})$ in the ν_{random}-inits (see black bars in top right panel). The vertical bar depicts the threshold radius r_{lb}.

Geosci. Model Dev. Discuss., doi:10.5194/gmd-2016-271, 2016
Manuscript under review for journal Geosci. Model Dev.
Published: 28 November 2016

Geoscientific Model Development Discussions
Open Access
EGU

init, the smallest ν-values occur only at the left and right tail of the DSD, whereas in the ν_{random}-approach the smallest ν-values (down to $\mathcal{N}\,10^{\alpha_{low}}$) can appear over the whole radius range. The horizontal bars in the plot indicate the values of α_{low},α_{med} and α_{high} and the vertical bar the threshold radius r_{lb}.

The second row shows average ν-value of all SIPs in a certain size bin. All init techniques are probabilistic and the average is taken over 50 independent realisations of SIP ensembles. Not surprisingly, the average ν of the ν_{draw}-method is identical to ν_{const}. Moreover, also for the ν_{random}-init the average ν-value is constant over a large radius range. Only in the right tail, the ν-values drop as intended. The third row shows the occurrence frequency of weighting factors.

To display DSDs represented by a SIP ensemble, a SIP ensemble must be converted back into a bin representation. For this, we establish a grid with resolution $\kappa_{plot} = 4$, count each SIP in its respective bin, i.e. SIP i with $m_{bb,l} < \mu_i \leq m_{bb,l+1}$ contributes to bin l via $M_{bin,l} = M_{bin,l} + \mu_i \times \nu_i$ and $n_{bin,l} = n_{bin,l} + \nu_i$. We note that all displayed DSDs in this study will use $\kappa = 4$, irrespective of the κ-value chosen in the initialisation. The fourth row shows such DSDs, again as an average over 50 SIP ensemble realisations. We find that any init technique is, in general, successful in producing a meaningful SIP ensemble as the "back"-translated DSD matches the originally prescribed DSD (black). Hence, the moments $\lambda_{k,SIP}$ match the analytical values $\lambda_{k,anal}$ for $0 \leq k \leq 3$, as shown in the fifth row. Nevertheless for the ν_{const}- and ν_{draw}-init, the spread between individual realisations can be large and they deviate substantially from the analytical reference. The singleSIP/multiSIP and ν_{random}, on the other hand, guarantee that each individual realisation is close to the reference.

2.2 Description of Hypothetical algorithm

First, we present a hypothetical algorithm for the treatment of collection/aggregation in an LCM, which would probably yield excellent results. However is prohibitively expensive in terms of computing power and memory, as N_{SIP} increases drastically over time until the state is reached where each SIP represents exactly one real droplet. Nevertheless, the presentation of this algorithm is useful for introducing several concepts which will partly occur in the subsequently described "real-world" algorithms.

Whereas condensation/deposition and sedimentation may be computed using interpolated quantities which implicitly assumes that all droplets of a SIPs are located at the same point, the numerical treatment of collection usually assumes that the droplets of a SIP are spatially uniformly distributed, i.e. well-mixed within the grid box. An approach, where the vertical SIP position is retained in the collection algorithm and larger droplets overtaking smaller droplets is explicitly modelled, is described in Sölch and Kärcher (2010), is not treated here.

Following Gillespie (1972) and Shima et al. (2009), the probability P_{ij} that one droplet with mass m_i collides with one droplet with mass m_j inside a small volume δV within a short time interval δt

Geosci. Model Dev. Discuss., doi:10.5194/gmd-2016-271, 2016
Manuscript under review for journal Geosci. Model Dev.
Published: 28 November 2016

Geoscientific Model Development Discussions
Open Access
EGU

is given by:

$$P_{ij} = K_{ij}\,\delta t\,\delta V^{-1}, \tag{9}$$

where $K_{ij} = K(m_i, m_j)$.

For SIPs i and j containing ν_i and ν_j real droplets in a grid box with volume ΔV, on average $\nu_{coll} = P_{ij}\,\nu_i\,\nu_j$ collections between droplets from SIP i and SIP j occur. The average rate of such $i-j$-collections ($i \neq j$) to occur is:

$$\frac{\partial \nu_{coll}(i,j)}{\partial t} = \nu_i\,K_{ij}\,\nu_j \Delta V^{-1} =: \nu_i o_{ij} =: O_{ij}. \tag{10}$$

So-called self-collections, collisions of the droplets belonging to the same SIP ($i = j$), are described by:

$$\frac{\partial \nu_{coll}(i,i)}{\partial t} = 2 \cdot \left(\frac{\nu_i}{2}\,K_{ii}\,\frac{\nu_i}{2}\Delta V^{-1}\right) = \frac{1}{2}\nu_i\,K_{ii}\,\nu_i \Delta V^{-1} =: \nu_i o_{ii} =: O_{ii}, \tag{11}$$

assuming that the SIP is split into two portions, each containing one half of the droplets of the original SIP. The factor of 2 originates from the collections of each half, which have to be added to gain the total number of self-collections for SIP i. Accordingly, the diagonal elements of the matrices o_{ij} and O_{ij} differ from the off-diagonal elements by an additional factor of 0.5. In terms of concentrations (represented by SIPs in a grid box with volume ΔV), we can write

$$\frac{\partial n_{coll}(i,j)}{\partial t} = K_{ij}\,n_i\,n_j \tag{12}$$

for collections between different SIPs and

$$\frac{\partial n_{coll}(i,i)}{\partial t} = \frac{1}{2}\,K_{ii}\,n_i^2 \tag{13}$$

for self-collections.

In the hypothetical algorithm, the weighting factor of SIP i is reduced due to collections with all other SIPs and self-collections and reads as

$$\frac{\partial \nu_i}{\partial t} = -\sum_{j=1}^{N_{SIP}} \frac{\partial \nu_{coll}(i,j)}{\partial t} = -\sum_{j=1}^{N_{SIP}} O_{ij}. \tag{14}$$

The droplet mass μ_i in SIP i is unchanged.

For each $i-j$-combination, a new SIP k is generated:

$$\frac{\partial \nu_k}{\partial t} = O_{ij} \quad \text{and} \quad \mu_k = \mu_i + \mu_j \tag{15}$$

To avoid double counting only combinations with $i \geq j$ are considered.

The rate equations for the weighting factors can be numerically solved by a simple Euler forward step: The weighting factor of existing SIPs is reduced by

$$\nu_i^{\Delta} := \left(\sum_{j=1}^{N_{SIP}} O_{ij}\right) \Delta t \tag{16}$$

Geosci. Model Dev. Discuss., doi:10.5194/gmd-2016-271, 2016
Manuscript under review for journal Geosci. Model Dev.
Published: 28 November 2016

Geoscientific Model Development Discussions
Open Access
EGU

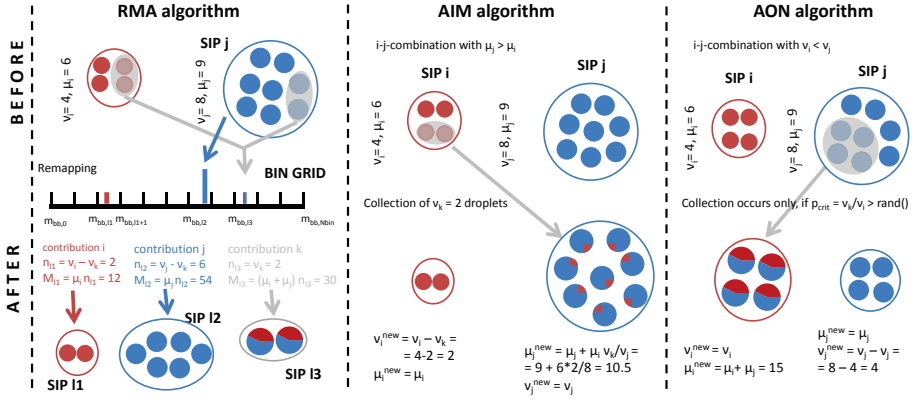

Figure 2. Treatment of a collection between two SIPs in the Remapping Algorithm (RMA), Average Impact Algorithm (AIM) and All-Or-Nothing Algorithm (AON).

leading to

$$\nu_i^* = \nu_i - \nu_i^{\Delta}, \tag{17}$$

or, equivalently,

$$\nu_i^* = \nu_i \left(1 - \Delta t \sum_{j=1}^{N_{SIP}} o_{ij}\right). \tag{18}$$

For new SIPs k we have

$$\nu_k = 0 + O_{ij} \cdot \Delta t. \tag{19}$$

Per construction the algorithm is mass-conserving subject to rounding errors.

In each time step, $N_{SIP,add} = N_{SIP}\,(N_{SIP} - 1)/2$ new SIPs are produced and the new number of SIPs is $N_{SIP}{}^* = N_{SIP} + N_{SIP,add}$. After nt time steps, the number of SIPs would be of order $(N_{SIP,0})^{nt}$ which is not feasible.

In the following subsections, algorithms are presented that include various approaches to keep the number of SIPs in an acceptable range.

In the following the various algorithms are described and pseudo-code of the implementations is given. For the sake of readability, the pseudo-code examples show easy-to-understand implementations. The actual codes of the algorithms are, however, optimised in terms of computational efficiency.

2.3 Description of the Remapping (RMA) algorithm

Geosci. Model Dev. Discuss., doi:10.5194/gmd-2016-271, 2016
Manuscript under review for journal Geosci. Model Dev.
Published: 28 November 2016

Geoscientific Model Development Discussions
Open Access
EGU

Algorithm 1 Pseudo-code of the Remapping algorithm

1: ***INIT BLOCK***
2: Given: Ensemble of SIPs; Specify: $\kappa, \eta, \Delta t$
3: **for** $l = 1$ **to** l_{max} **do** *{Create temporary bin}*
4: $m_{bin,l} = m_{bin,low} 10^{l/\kappa}$
5: **end for**
6: ***TIME ITERATION***
7: **while** t<Tsim **do**
8: ***LOSS BLOCK*** *{Compute reduced bin contribution of existing SIPs}*
9: **for** $i = 1$ **to** N_{SIP} **do**
10: Calculate ν_i^* according to Eq. 18
11: Select bin l with $m_{bb,l} < \mu_i \leq m_{bb,l+1}$
12: $n_{bin,l} = n_{bin,l} + \nu_i^*$
13: $M_{bin,l} = M_{bin,l} + \nu_i^* \cdot \mu_i$
14: **end for**
15: ***GAIN BLOCK*** *{Compute bin contribution of coalescing droplets}*
16: **for all** $i < j \leq N_{SIP}$ **do**
17: k++
18: Compute ν_k according to Eq. 19
19: $\mu_k = \mu_i + \mu_j$
20: Select bin l with $m_{bb,l} < \mu_k \leq m_{bb,l+1}$
21: $n_{bin,l} = n_{bin,l} + \nu_k$
22: $M_{bin,l} = M_{bin,l} + \nu_k \cdot \mu_k$
23: **end for**
24: ***CREATE BLOCK*** *{Replace SIPs}*
25: Delete all SIPs
26: **for all** l with $M_{bin,l} > M_{critmin} = \eta\lambda_1$ **do** *{use $M_{critmin}$ as a weak threshold value}*
27: i++
28: Generate SIP i with $\nu_i^{new} = n_{bin,l}$ and $\mu_i = M_{bin,l}/\nu_{bin,l}$
29: **end for**
30: $N_{SIP} = ii$
31: $t = t + \Delta t$
32: **end while**
33: ***EXTENSIONS***
34: *Self-collections for a kernel with $K(m,m) \neq 0$ can be easily incorporating in the algorithm by changing the condition in line 16 to $i \leq j \leq N_{SIP}$.*

Geosci. Model Dev. Discuss., doi:10.5194/gmd-2016-271, 2016
Manuscript under review for journal Geosci. Model Dev.
Published: 28 November 2016

Geoscientific Model Development Discussions
Open Access
EGU

First, the remapping algorithm is described as its concept follows closely the hypothetical algorithm introduced in the latter section. The RMA algorithm is based on ideas of Andrejczuk et al. (2010). We call their approach 'remapping algorithm' as N_{SIP} is kept reasonably low by switching between a SIP representation and a bin representation in every time step. A temporary bin grid with a pre-defined κ is established which stores the total number $n_{bin,*}$ and total mass $M_{bin,*}$ of all contributions belonging to a specific bin. The bin boundaries are given by $m_{bb,*}$.

Instead of creating a new SIP k (with number ν_k obtained by Eq. 15 and mass $\mu_k = \mu_i + \mu_j$) from each $i-j$-combination, the according contribution is stored on a temporary bin grid. More explicitly, this means that the droplet number $n_{bin,l}$ of bin l with $m_{bb,l} < \mu_k \leq m_{bb,l+1}$ is increased by ν_k. Similarly, the total mass $M_{bin,l}$ of that bin is increased by $\mu_k \nu_k$. Similarly, the reduced contributions ν_i^* from the existing SIPs with droplet mass μ_i are added to their respective bins.

Figure 2 illustrates how a collection process between two SIPs is treated in RMA. In this example, $\nu_k = 2$ droplets are produced by collection which have a droplet mass of $\mu_k = \mu_i + \mu_j = 15$. Instead of creating a new SIP k (as in the hypothetical algorithm), the contribution k is recorded in the bin grid. The droplet number n in bin $l3$ is increased by $\nu_k = 2$ and the according total mass M_{l3} by $\nu_k \mu_k = 30$. The remaining contribution of SIP i falls into bin $l1$ and n_{l1} and M_{l1} are increased by $\nu_i^* = \nu_i - \nu_k = 2$ and $\mu_i \nu_i^* = 12$, respectively. The operation for SIP j is analogous.

At the end of each time step after treating all possible $i-j$-combinations, a SIP ensemble is created from the bin data with $\nu_i = n_{bin,l}$ and $\mu_i = M_{bin,l}/n_{bin,l}$.

Optionally, a lower threshold $\nu_{min,RMA}$ can be introduced, such that SIP i is created only if $n_{bin,l} > \nu_{min,RMA}$ holds. However, this may destroy the property of mass conservation which can be remedied by the following.

We pick up the concept of a weak threshold introduced earlier and adjust it such that on average the total mass is conserved (instead of total number as before). We introduce the threshold $M_{critmin} = \eta \lambda_1$. E.g. η is set to 10^{-10}, which implies that each SIP contains at least 10^{-10} of the total mass in a grid box. If $M_{bin,l} > M_{critmin}$, a SIP is created representing $\nu_i = n_{bin,l}$ drops with single mass $\mu_i = M_{bin,l}/n_{bin,l}$. If $M_{bin,l} < M_{critmin}$, a SIP is created with probability $p_{create} = M_{bin,l}/M_{critmin}$. In this case the SIP represents $\nu_i = M_{critmin}/\mu_i$ droplets with single mass $\mu_i = M_{bin,l}/n_{bin,l}$. Pseudo-code of the algorithm is given in algorithm 1.

Time steps typically used in previous collection/aggregation tests are around $\Delta t = 0.1$ to $10\,\mathrm{s}$ depending inter alia on the used kernel. From Eq. 18 follows that the time step in RMA must satisfy

$$\Delta t < \sum_{j=1}^{N_{SIP}} o_{ij}. \tag{20}$$

Otherwise, negative ν-values can occur which would inevitably lead to a crash of the simulation. In mature clouds, the Long and Hall kernel attain large values which required tiny time steps of $10^{-4}\,\mathrm{s}$ and smaller in the first test simulations. To be of any practical relevance, RMA had to be modified in order to be able to run simulations with suitable time steps.

Geosci. Model Dev. Discuss., doi:10.5194/gmd-2016-271, 2016
Manuscript under review for journal Geosci. Model Dev.
Published: 28 November 2016

Geoscientific Model Development Discussions
Open Access
EGU

Hence, several extensions to RMA allowing larger time steps are discussed in the following.

1. *Default version:* Use the algorithm as outlined in Algorithm 1 (i.e. do not change anything). Negative ν_i^*-values obtained by Eq. 17 are acceptable, as long as $n_{bin,l}$, from which the SIPs are created at the end of the time iteration, is non-negative for all l. This means that an existing SIP i (which falls into bin l) can lose more droplets (ν_i^Δ) than it actually possesses (ν_i) as long as the gain in bin l (from all suitable SIP combinations) compensates this deficit. We will later see that this approach works well for the Golovin kernel, however fails for the Long and Hall kernel.

2. *Clipping:* Simply ignore bins with negative $n_{bin,l}$ and do not create SIPs from those bins. This approach destroys the property of mass conservation and is not pursued here.

3. *Adaptive time stepping:* Instead of reducing the general time step, only the treatment of SIPs with $\nu_i^* < 0$ is sub-cycled. For each such SIP i, Eq. 17 is iterated $\tilde{\eta}_i$ times with time step $\Delta t_{SIP} = \Delta t/\tilde{\eta}_i$. Note that even though the computation of Eq. 17 and O_{ij} involves the ν-evaluation of all SIPs, only ν_i is updated in the subcycling steps and not the whole system of fully coupled equations is solved for a smaller time step. For sufficiently large $\tilde{\eta}_i$, $\nu^*_{i,subcycl}$ is positive, as $\nu^\Delta_{i,subcycl} < \nu_i$ as desired. Basically, we now assume that all collections involving SIP i are equally reduced by a factor of $\eta_i = \nu^\Delta_{i,subcycl}/\nu_i^\Delta$ compared to the default time step. In the GAIN block of the algorithm (as termed in Alg. 1), all computations use the default time step and no sub-cycling is applied. To be consistent with the reduction in the LOSS block, Eq. 19 is replaced by $\nu_k = \eta_i O_{ij} \Delta t$.

4. *Reduction limiter* The effect of an adaptively reduced time step can be reached with simpler and cheaper means. We introduce a threshold parameter $0 < \tilde{\gamma} < 1.0$ similar to the approach in Andrejczuk et al. (2012). Again, we focus on SIPs with $\nu_i^* < 0$ and simply set the new weight of SIP i to $\nu^*_{i,RedLim} = \tilde{\gamma}\nu_i$. As above, all contributions involving SIP i have to be re-scaled, now with $\gamma_i = (\nu_i - \nu^*_{i,RedLim})/\nu_i^\Delta$.

5. *Update on the fly* Another option to eliminate negative ν_i-values is to do an "update on the fly". In this case, the algorithm is not separated in a LOSS and GAIN block. Instead, the $i-j$-combinations are processed one after another. After each collection process, as exemplified in Fig. 2, the weighting factors ν_i and ν_j of the two involved SIPs are reduced by ν_k, i.e. the number of droplets that were collected. Subsequent evaluations of Eq. 19 then use updated ν-values. Compared to the default version, it now matters in which order the $i-j$-combinations are processed, e.g. if you deal first with combinations of the smallest SIPs or of the largest SIPs.

2.4 Description of Average Impact (AIM) algorithm

Geosci. Model Dev. Discuss., doi:10.5194/gmd-2016-271, 2016
Manuscript under review for journal Geosci. Model Dev.
Published: 28 November 2016

Geoscientific Model Development Discussions
Open Access
EGU

Algorithm 2 Pseudo-code of the average impact algorithm

1: ***INIT BLOCK + SIP SORTING***
2: Given: Ensemble of SIPs; Specify: Δt
3: ***TIME ITERATION***
4: **while** t<Tsim **do**
5: *{Sort SIPs by droplet mass}*
6: Apply (adaptive) sorting algorithm, such that $\mu_j \geq \mu_i$ for $j > i$
7: *{Compute total mass χ_i of each SIP}*
8: $\chi_i = \nu_i \, \mu_i$
9: **for** $i = 1$ **to** N_{SIP} **do**
10: *{Compute reduction of weighting factor due to number loss to all larger SIPs}*
11: $\nu_i^{new} = \nu_i \left(1 - \Delta t \sum_{j=i+1}^{N_{SIP}} o_{ij}\right)$
12: *{Compute mass transfer; mass gain from all smaller SIPs and mass loss to all larger SIPs}*
13: $\chi_i^{new} = \chi_i - \chi_i \Delta t \sum_{j=i+1}^{N_{SIP}} o_{ij} + \sum_{j=1}^{i-1} \chi_j o_{ij} \Delta t$
14: **end for**
15: $\nu_i = \nu_i^{new}$
16: $\mu_i = \chi_i^{new} / \nu_i^{new}$
17: $t = t + \Delta t$
18: **end while**
19: ***EXTENSIONS***
20: *{Self-collections for a kernel with $K_{ii} \neq 0$ can be incorporated simply by adding the term $-0.5 \, \Delta t \, o_{ii}$ inside the bracket on the r.h.s. of line 11 (see also Eq. (23) in the text)}*

The average impact algorithm by Riechelmann et al. (2012) and further developed in Maronga et al. (2015) predicts the temporal change of the weighting factor, ν_i, and the total mass of all droplets represented by each SIP, $\chi_i = \nu_i \, \mu_i$. In this algorithm, two fundamental interactions of droplets are considered (see also Fig. 7 in Maronga et al., 2015). First, the coalescence of two SIPs of different size. It is assumed that the larger SIP collects a certain amount of the droplets represented by the smaller SIP, which is then equally distributed among the droplets of the larger SIP. As a consequence, the total mass and the weighting factor of the smaller SIP decrease, while the total mass of the larger SIP increases accordingly. Fig. 2 illustrates how a collection between two SIPs is treated. SIP j is assumed to represent larger droplets than SIP i, i.e. $\mu_j > \mu_i$. As in the RMA example before, we say that $\nu_k = 2$ droplets are collected. Then SIP i loses two droplets to SIP j, i.e. ν_i is reduced by 2 and a mass of $\mu_i \nu_k$ is transferred to SIP j where it is distributed among the existing $\nu_j = 8$ droplets. Unlike to RMA, where droplets with mass $\mu_j + \mu_i = 15$ are produced, AIM predicts a droplet mass of $\mu_j + \mu_i \nu_k / \nu_i = 10.5$ in SIP j. Usually, $\nu_k / \nu_i << 1$ and hence the name "average impact" for this algorithm.

Geosci. Model Dev. Discuss., doi:10.5194/gmd-2016-271, 2016
Manuscript under review for journal Geosci. Model Dev.
Published: 28 November 2016

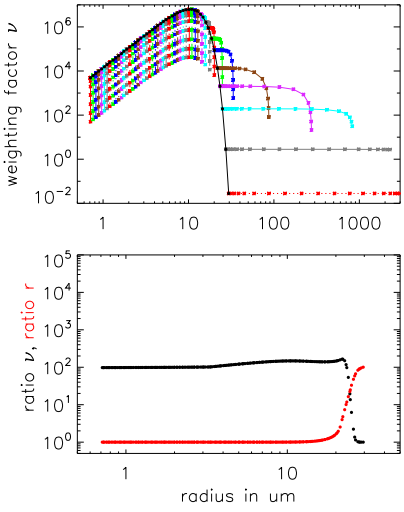

Figure 3. top: (r_i, ν_i)-evolution of selected SIPs. The black line shows the initial distribution. Each coloured line connects the data points that depict the (r_i, ν_i)-pair of an individual SIP every 200 s.
bottom: Ratios $r_i(t = 3600\,\mathrm{s})/r_i(t = 0\,\mathrm{s})$ (red curve) and $\nu_i(t = 0\,\mathrm{s})/\nu_i(t = 3600\,\mathrm{s})$ (black curve) for all SIPs as a function their initial radius $r_i(t = 0\,\mathrm{s})$.
An example simulation with Long kernel, singleSIP-init, $\Delta t = 10\,\mathrm{s}, \kappa = 40$ and $N_{SIP} = 197$ is displayed.

Moreover, same-size collisions are considered in each SIP. This decreases the weighting factor of each SIP but not its total mass. Accordingly, the radius of the SIP increases.

Both processes are represented in the following two equations which are solved for all colliding SIPs (assuming that $\mu_0 \leq \mu_1 \leq \ldots \leq \mu_{N_{SIP}}$):

$$\frac{\mathrm{d}\nu_i}{\mathrm{d}t} = -K_{ii}\,\frac{1}{2}\,\frac{\nu_i \nu_i}{\Delta V} - \sum_{j=i+1}^{N_{SIP}} K_{ij}\nu_i\nu_j\Delta V^{-1} \tag{21}$$

and

$$\frac{\mathrm{d}\chi_i}{\mathrm{d}t} = \sum_{j=1}^{i-1} \mu_j\, K_{ij}\nu_i\nu_j\Delta V^{-1} - \mu_i \sum_{j=i+1}^{N_{SIP}} K_{ij}\nu_i\nu_j\Delta V^{-1}. \tag{22}$$

The first term on the right-hand-side of Eq. 21 describes the decrease of ν due to same-size collections, the second term the decrease of ν due to collection by larger SIPs. The first term on the right-hand-side of Eq. 22 describes the gain in total mass due to collections with smaller SIPs, while the second term describes the loss of total mass due to collection by larger SIPs.

Using a Euler forward method for time integration the above equations read as:

$$\nu_i^{new} = \nu_i \left(1 - \sum\nolimits_{j=i+1}^{N_{SIP}} o_{ij}\Delta t - 0.5\, o_{ii}\Delta t\right) \tag{23}$$

Geosci. Model Dev. Discuss., doi:10.5194/gmd-2016-271, 2016
Manuscript under review for journal Geosci. Model Dev.
Published: 28 November 2016

and

$$\chi_i^{new} = \chi_i \left(1 - \sum_{j=i+1}^{N_{SIP}} o_{ij} \Delta t\right) + \sum_{j=1}^{i-1} \chi_j o_{ij} \Delta t. \quad (24)$$

Finally, the mass μ_i of each SIP is updated: $\mu_i^{new} = \chi_i^{new} / \nu_i^{new}$.

Figure 2 illustrates how the AIM algorithm works for an example simulation with the Long kernel and singleSIP-init. The top panel shows the (r_i, ν_i)-evolution of selected SIPs. The black line shows the initial distribution. Each coloured line connects the data points that depict the (r_i, ν_i)-pair of an individual SIP every 200 s. Clearly, ν_i of any SIP decreases over time, however the decrease is much smaller for the largest SIPs and becomes zero for the largest SIP. The majority of SIPs starting from the smallest radii show an opposite behaviour as their evolution is dominated by a strong ν_i-decrease at nearly constant r_i. In contrast, the evolution of the two largest SIPs is dominated by a strong r_i-increase for constant ν_i. The SIPs next to the largest SIPs undergo a transition; in the beginning, they primarily grow in size, towards the end the decrease of ν_i is dominant. The bottom panel shows the ratios $r_i(t = 3600\,\mathrm{s})/r_i(t = 0\,\mathrm{s})$ (red curve) and $\nu_i(t = 0\,\mathrm{s})/\nu_i(t = 3600\,\mathrm{s})$ (black curve) for all SIPs of the simulation. Both ratios are smooth functions of the initial r_i which is plotted on the x-axis.

By construction, the number of SIPs remains constant over the course of a simulation. Hence, the number of SIPs per radius or mass interval decreases, when the DSD broadens over time. In our example, the SIP resolution becomes coarser, particularly in the large droplet tail.

Negative values of ν_i^{new} and χ_i^{new} may occur. However, this case never occurred in our manifold tests of the algorithm. The behaviour appears more benign than in RMA. Moreover, we found that the algorithm preserved the initial size-sortedness of the SIP ensemble. However, for an arbitrary kernel function and initial SIP ensemble, this is not guaranteed and we recommend to use adaptive sorting algorithms that benefit from partially pre-sorted data sets (Estivill-Castro and Wood, 1992). Adaptive sorting is also advantageous, when AIM is employed in real world applications, where sedimentation, advection and condensation changes the SIP ensemble in each individual grid box.

2.5 Description of the All-Or-Nothing (AON) algorithm

The All-Or-Nothing (AON) algorithm is based on the ideas of Sölch and Kärcher (2010) and Shima et al. (2009). Fig. 2 illustrates how a collection between two SIPs is treated. SIP i is assumed to represent fewer droplets than SIP j, i.e. $\nu_i < \nu_j$. Each real droplet in SIP i collects one real droplet from SIP j . Hence, SIP i contains $\nu_i = 4$ droplets, now with mass $\mu_i + \mu_j = 15$. SIP j now contains $\nu_j - \nu_i = 8 - 4 = 4$ droplets with mass $\mu_j = 9$. Following Eq. 19, only $\nu_k = 2$ pairs of droplets would, however, merge in reality. The idea behind this probabilistic AON algorithm is that such a collection event is realised only under certain circumstances in the model, namely such that the expectation values of collection events in the model and in the real world are the same. This is achieved if a collection event occurs with probability $p_{crit} = \nu_k / \nu_i$ in the model. Then, the average number of

Geosci. Model Dev. Discuss., doi:10.5194/gmd-2016-271, 2016
Manuscript under review for journal Geosci. Model Dev.
Published: 28 November 2016

Geoscientific Model Development Discussions
Open Access
EGU

Algorithm 3 Pseudo-code of the all-or-nothing algorithm; rand() generates uniformly distributed random numbers $\in [0,1]$.

1: ***INIT BLOCK***
2: Given: Ensemble of SIPs; Specify: Δt
3: ***TIME ITERATION***
4: **while** t<Tsim **do**
5: *{Check each $i-j$-combination for a possible collection event}*
6: **for all** $i < j \leq N_{SIP}$ **do**
7: Compute ν_k according to Eq. 15
8: $\nu_{new} = \min(\nu_i, \nu_j)$
9: $p_{crit} = \nu_k / \nu_{new}$
10: *{Update SIP properties on the fly}*
11: **if** $p_{crit} > 1$ **then**
12: ***MULTIPLE COLLECTION***
13: *{can occur when ν_i and ν_j differ strongly and be regarded as special case; see text for further explanation}*
14: assume $\nu_i < \nu_j$, otherwise swap i and j in the following lines
15: *{$p_{crit} > 1$ is equivalent to $\nu_k > \nu_i$}*
16: *{transfer ν_k droplets with μ_j from SIP j to SIP i, allow multiple collections in SIP i, i.e. one droplet of SIP i collects more than one droplet of SIP j.}*
17: SIP i collects ν_k droplets from SIP j and distributes them on ν_i droplets: $\mu_i = (\nu_i \mu_i + \nu_k \mu_j)/\nu_i$
18: SIP j loses ν_k droplets to SIP i: $\nu_j = \nu_j - \nu_k$
19: **else if** p_{crit} >rand() **then**
20: ***RANDOM SINGLE COLLECTION***
21: assume $\nu_i < \nu_j$, otherwise swap i and j in the following lines
22: *{transfer ν_i droplets with μ_j from SIP j to SIP i}*
23: SIP i collects ν_i droplets from SIP j: $\mu_i = \mu_i + \mu_j$
24: SIP j loses ν_i droplets to SIP i: $\nu_j = \nu_j - \nu_i$
25: **end if**
26: **end for**
27: $t = t + \Delta t$
28: **end while**
29: ***EXTENSIONS***
30: *{Self-collections for a kernel with $K(m,m) \neq 0$ can be treated in the following way: }*
31: *{Insert the following loop before line 6 or after line 26.}*
32: **for** $i = 1$ **to** N_{SIP} **do**
33: $p_{crit} = \nu_k / \nu_i$
34: **if** $2\, p_{crit}$ >rand() **then**
35: *{every two (identical) droplets coalesce}*
36: $\nu_i = \nu_i / 2$
37: $\mu_i = 2\, \mu_i$
38: **end if**
39: **end for**

Geosci. Model Dev. Discuss., doi:10.5194/gmd-2016-271, 2016
Manuscript under review for journal Geosci. Model Dev.
Published: 28 November 2016

Geoscientific Model Development Discussions
Open Access
EGU

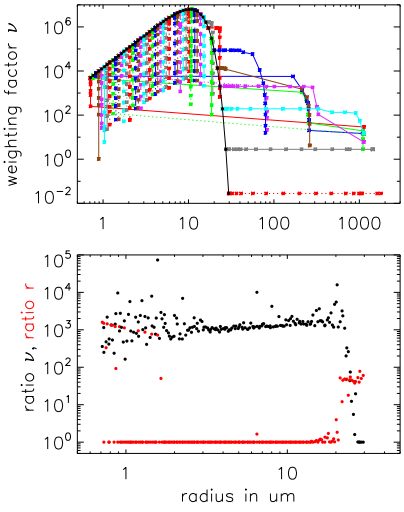

Figure 4. As in Fig. 3, for the AON algorithm.

collections in the model,

$$\bar{\nu}_k = p_{crit}\nu_i = (\nu_k/\nu_i)\nu_i,$$

is equal to ν_k as in the real world. A collection event between two SIPs occurs, if p_{crit} >rand(). The function rand() provides uniformly distributed random numbers $\in [0,1]$.

Noticeably, no operation on the SIPs is performed if p_{crit} <rand().

The treatment of the special case $\nu_k/\nu_i > 1$ needs some clarification. This case is regularly encountered when the singleSIP-init is used, where SIPs with large droplets and small ν_i collect small droplets from a SIP with large ν_j. The large difference in droplet masses μ lead to large kernel values and high ν_k with $\nu_i < \nu_k < \nu_j$. By the way, the case of ν_k being even larger than ν_j is not considered, as it occurs only with unrealistically large time steps. If $p_{crit} > 1$, we allow multiple collections, as each droplet in SIP i is allowed to collect more than one droplet from SIP j. In total, SIP i collects ν_k droplets from SIP j and distributes them on ν_i droplets. A total mass of $\nu_k\mu_j$ is transferred from SIP j to SIP i and the droplet mass in SIPs i becomes $\mu_i^{new} = (\nu_i\,\mu_i + \nu_k\,\mu_j)/\nu_i$. The number of droplets in SIP j is reduced by ν_k and $\nu_j^{new} = \nu_j - \nu_k$. Sticking to the example in Fig. 2 and assuming $\nu_k = 5$, each of the $\nu_i = 4$ droplets would collect $\nu_k/\nu_i = 1.25$ droplets. The properties of SIP i and SIP j are then: $\nu_i = 4$, $\mu_i = 17.25$, $\nu_j = 3$ and $\mu_j = 9$.

Another special case appears if both SIPs have the same weighting factor which regularly occurs when the ν_{const}-init is used. After a collection event, SIP j would carry $\nu_j - \nu_i = 0$ droplets, whereas SIP i would still represent ν_i droplets. In this case, half of the droplets from SIP i are moved to SIP j and both SIPs carry $\nu_j^{new} = \nu_i^{new} = 0.5\nu_i$ droplets with mass $\mu_i + \mu_j$. Without this correction,

Geosci. Model Dev. Discuss., doi:10.5194/gmd-2016-271, 2016
Manuscript under review for journal Geosci. Model Dev.
Published: 28 November 2016

zero-ν SIPs would accumulate over time and reduce the effective number of SIPs causing a poorer sampling. Instead of this equal splitting, one can also assign unequal shares $\xi\,\nu_i$ and $(1-\xi)\nu_i$ to the two SIPs (with ξ being some random number).

Moreover, self-collections can be considered for kernels with $K_{ii} > 0$. If 2 p_{crit} >rand(), self-collections occur between the droplets in a SIP (note the factor 2 due to symmetry reasons). Then every two droplets within a SIP coalesce, implying $\nu_i = \nu_i/2$ and $\mu_i = 2\,\mu_i$.

So far, we explained how a single $i-j$-combination is treated in AON. In every time step, the full algorithm simply checks each $i-j$-combination for a possible collection event. To avoid double-counting only combinations with $i < j$ and self-collections with $i = j$ are considered. Pseudo-code of the algorithm is given in Algorithm 3. The SIP properties are updated on the fly. If a certain SIP is involved in a collection event in the model and changes its properties, all subsequent combinations with this SIP take into account the updated SIP properties. Similar to the update on the fly version of RMA, results may depend on the order in which the $i-j$-combinations are processed.

For most $i-j$-combinations, p_{crit} is small and usually only a limited number of collection events occurs in the model and AON may suffer from an insufficient sampling of the droplet space. Actual collections are a rare event in this algorithm. In our standard setup, $< 1\%$ of all possible collections occur in the model until rain is initiated by very few lucky SIPs (similar to lucky drops, e.g. Kostinski and Shaw (2005)). Indeed, Shima et al. (2009) reported convergence of AON only for tremendously many SIPs (on the order of 10^5 to 10^6 in a box). We will later see that convergence is possible with as few as $O(10^2)$ SIPs, if the SIPs are suitably initialised. Hence, it will be demonstrated that AON is a viable option in 2D/3D cloud simulations, as already implied in Arabas and Shima (2013).

As for AIM in Fig. 3, Fig. 4 (top) shows the (r_i, ν_i)-evolution of selected SIPs for AON. The picture looks more chaotic than for AIM, as each individual SIP has its own independent history due to the probabilistic nature of AON. For the initially smallest SIP, only ν_i changes for most of the time, as only collections occur where the partner SIPs have smaller weighting factors ν. Towards the end, the still very small SIP is at least once involved in a collection with a very large SIP that has a larger ν. Hence, r_i of this SIP increases substantially. In contrast to the smallest SIP, other initially small SIPs i with similar properties are never part of a collection with $\nu_i < \nu_j$. Hence, their radii r_i remain small over the total period and ν_i is the only property that changes. The bottom panel summarises the overall changes in ν_i (black) and r_i (red) for all SIPs of the simulation. Unlike to AIM, where only the initially largest SIPs grow, SIPs from both ends of the spectrum grow in AON. Those SIPs have small ν-values in common and in each collection their mass is updated to $m_i + m_j$. The SIPs with initially large ν-values lie in the radius range $[2\,\mu\mathrm{m}, 15\,\mu\mathrm{m}]$ and keep their initial radii (at least in the singleSIP-init used here). The reductions in ν_i scatter around $\sim 10^3$ for most SIPs and fall off to 1 for the largest SIPs.

Geosci. Model Dev. Discuss., doi:10.5194/gmd-2016-271, 2016
Manuscript under review for journal Geosci. Model Dev.
Published: 28 November 2016

Geoscientific Model Development Discussions
Open Access
EGU

For the generation of the random numbers, the well-proven (L'Ecuyer and Simard, 2007) Mersenne Twister algorithm by Matsumoto and Nishimura (1998) is used. AON simulations may be accelerated if random numbers are computed once a priori. However, this requires saving millions of random numbers for every realisation. An AON simulation with 1000 time steps and 200 SIPs implying 200×100 combinations, e.g. processes $2 \cdot 10^7$ random numbers. Using random numbers with a smaller cycle length deteriorated the simulation results in several tests and is not recommended.

The current implementation differs slightly from the version in Shima et al. (2009). Due to an unfavourable SIP initialisation similar to the ν_{const}-technique, Shima et al. (2009) deal with large N_{SIP}-values in their simulations, where it becomes prohibitive to evaluate all $N_{SIP}(N_{SIP}-1)$ SIP-combinations. Hence, they resort to $\lfloor N_{SIP}/2 \rfloor$ randomly picked $i-j$-combinations, where each SIP appears exactly in one pair (if N_{SIP} is odd, one SIP is ignored). As only a subset of all possible combinations are numerically evaluated, the extent of collisions is underestimated. To compensate for this, the probability p_{crit} is up-scaled with a scaling factor $N_{SIP}(N_{SIP}-1)/(2\,\lfloor N_{SIP}/2 \rfloor)$ to guarantee an expectation value as desired.

Moreover, in Shima's formulation the weighting factors are considered to be integer numbers. In contrast, we use real numbers ν which can even attain values below 1.0. This has several computational advantages: 1. better sampling of the DSD, in particular at the tails, 2. simpler AON implementation with fewer arithmetic and rounding operations, and 3. more flexibility, e.g. SIP splitting with real-valued ξ in the case of identical weighting factors.

Sölch and Kärcher (2010) makes use of the vertical position of the SIPs and explicitly calculates whether or not a larger droplet overtakes a smaller droplet within a time step. This approach will be thoroughly analysed in a follow-up study.

In RMA and AIM SIPs with negative weights may be generated depending, e.g. on the condition $\Delta t \sum_{j=1}^{N_{SIP}} o_{ij} > 1$ in RMA. In AON, the latter condition implies that $\sum_{j=1} p_{crit,ij}$ of SIP i is greater than unity. Hence, this SIP is likely to be involved in several collections (for j with $p_{crit,ij} < 1$) or is involved in one or several multiple collections (for j with $p_{crit,ij} > 1$).

3 Box model results

In this section, box model simulations of the three algorithms introduced in the latter section are presented, starting with the results of the Remapping (RMA) Algorithm, then those of the Average Impact (AIM) and finally the All-or-Nothing (AON) algorithm. The results of each algorithm are tested for three different collection kernels (Golovin, Long and Hall). Simulations with the Golovin kernel are compared against the analytical solution given by Golovin (1963). Consistent with many previous studies we choose $b = 1.5\ \mathrm{m^3\,kg^{-1}\,s^{-1}}$.

Simulations with the Long and Hall kernel are compared against high-resolution benchmark simulations obtained by the spectral-bin model approaches of Wang et al. (2007) and Bott (1998). In all

Geosci. Model Dev. Discuss., doi:10.5194/gmd-2016-271, 2016
Manuscript under review for journal Geosci. Model Dev.
Published: 28 November 2016

Geoscientific Model Development Discussions
Open Access
EGU

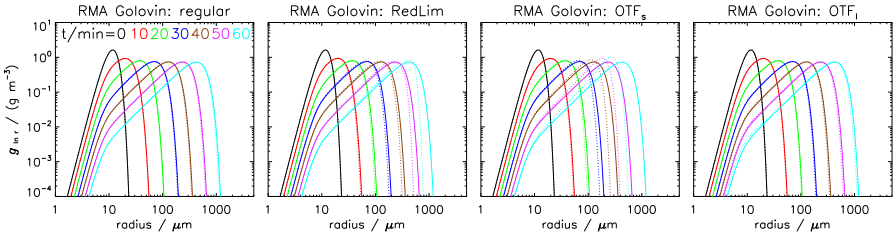

Figure 5. Mass density distributions obtained by the RMA algorithm for the Golovin kernel from $t = 0$ to $60\,\mathrm{min}$ every $10\,\mathrm{min}$ (from black to cyan). The solid curves show the reference solution, the dotted curves the simulation result of the RMA algorithm. The parameter settings are probabilistic singleSIP-init with weak threshold, $\kappa = 60$, $\eta = 10^{-8}$ and $\Delta t = 1\,\mathrm{s}$. The following versions of the RMA algorithm are depicted (from left to right): regular version, version with reduction limiter, version with update on the fly (start with combinations of smallest/largest droplets).

simulations, collision/coalescence is the only process considered in order to enable a rigorous evaluation of the algorithms. The evaluation is based on the comparison of mass density distributions, and the temporal development of 0th, 2nd, and 3rd moment of the droplet distributions. The 1st moment is not shown since the mass is conserved in all algorithms per construction.As default, probabilistic SIP initialisation methods are used. For each parameter setting, simulations are performed for 50 different realisations.

3.1 Performance of Remapping (RMA) Algorithm

Figure 5 compares DSDs of the RMA algorithm and the analytical reference solution for the Golovin kernel. Each panel displays DSDs from $t = 0$ to $60\,\mathrm{min}$ every $10\,\mathrm{min}$. The left panel shows an excellent agreement of RMA with the reference solution and proves at least a correct implementation. Figure 6 compares the temporal evolution of the moments. Moreover, the first row shows the number of SIPs used in RMA. Except for the case with a very coarse grid ($\kappa = 5$) with fewer than 40 SIPs in the end, the RMA results agree perfectly with the reference solution irrespective of the chosen κ (≥ 10) and minimum weak threshold η ranging from 10^{-5} to 10^{-8}. The number of non-zero bins increases as the DSD broadens over time. In the last step of the time iteration, SIPs are created from such bins. Hence, their number increases over time. Using a strict threshold, the total mass is not conserved (not shown); The larger η is, the more mass is lost. Hence, using a weak threshold or some other measure (e.g. creation of a residual SIP containing contributions of all neglected bins) to avoid this is highly recommended.

Next, RMA simulations with the Long kernel are discussed. As already mentioned, the default RMA version would require tiny time steps which would rule out RMA from any practical application. Both approaches introduced before, "Update on the fly" and "Reduction Limiter", succeed

Geosci. Model Dev. Discuss., doi:10.5194/gmd-2016-271, 2016
Manuscript under review for journal Geosci. Model Dev.
Published: 28 November 2016

Geoscientific Model Development Discussions
Open Access
EGU

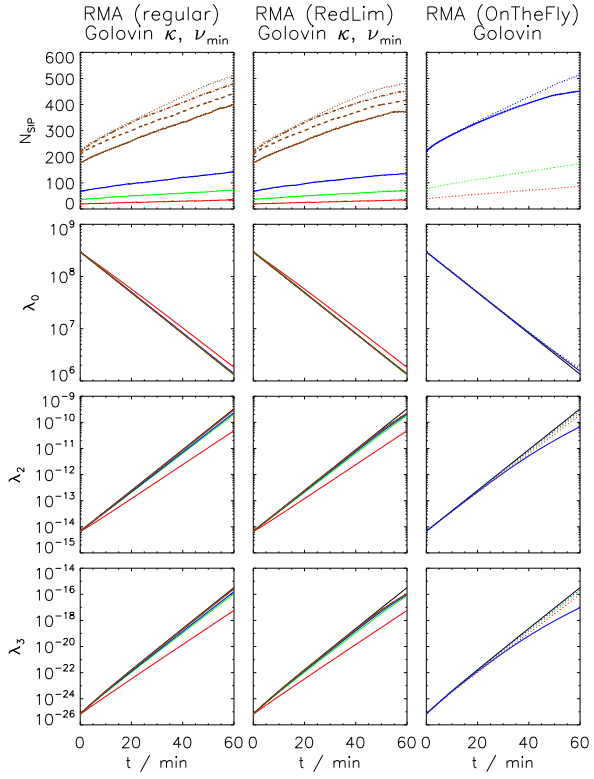

Figure 6. SIP number and moments λ_0, λ_2 and λ_3 as a function of time obtained by the RMA algorithm for the Golovin kernel. The black curves show the moments of the reference solution. All other curves depict the RMA results. The default settings are: Probabilistic singleSIP-init with weak threshold and $\Delta t = 1\,\mathrm{s}$. Left column: regular version with $\kappa = 60$, 20, 10, 5 (brown, blue, green, red) and threshold $\eta = 10^{-5}$, 10^{-6}, 10^{-7}, 10^{-8} (solid, dashed, dash-dotted, dotted). Middle column: as in left column, but version with reduction limiter. Right column: version with update on the fly, solid/dotted lines: start with combinations of smallest/largest droplets, colours as before.

Geosci. Model Dev. Discuss., doi:10.5194/gmd-2016-271, 2016
Manuscript under review for journal Geosci. Model Dev.
Published: 28 November 2016

Geoscientific Model Development Discussions
Open Access
EGU

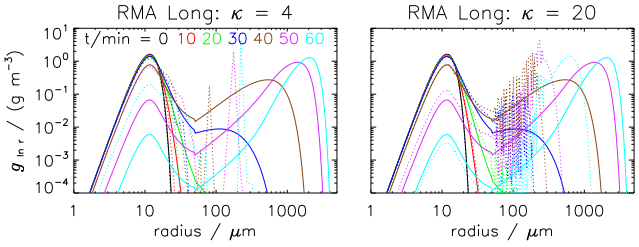

Figure 7. Mass density distributions obtained by the RMA algorithm for the Long kernel from $t = 0$ to $60\,\mathrm{min}$ every $10\,\mathrm{min}$ (from black to cyan). The solid curves show the reference solution, the dotted curves the simulation result of the RMA algorithm with Reduction Limiter ($\tilde{\gamma} = 0.1$). The parameter settings are probabilistic singleSIP-init with weak threshold, $\eta = 10^{-8}$, $\Delta t = 0.1\,\mathrm{s}$ and $\kappa = 4$ or 20 (as indicated on top).

in eliminating negative ν_i-values and in finishing the simulation within a reasonable time. However, the results are not as desired. Fig. 7 shows the DSDs for a simulation with Reduction Limiter, weak threshold $\eta = 10^{-8}$ and parameters $\kappa = 60$, $\Delta t = 0.1\,\mathrm{s}$ and $\tilde{\gamma} = 0.1$. Whereas the algorithm is capable of realistically reducing the number of the smaller droplets, it fails to predict the formation of the rain mode and strong oscillations appear in the intermediate radius range $[100\,\mu\mathrm{m}, 200\,\mu\mathrm{m}]$. We tested the algorithm with many parameter settings varying all of the aforementioned parameters, $\Delta t \in [0.1\,\mathrm{s}, 1\,\mathrm{s}], \kappa \in [10, 60], \tilde{\gamma} \in [0, 1]$ and $\eta \in [10^{-10}, 10^{-5}]$. Unfortunately, spurious oscillations occur in most cases. Integrating over the whole mass spectrum, those oscillations do not average out and, not surprisingly, the moments do not come close to the reference solution (not shown). Non-oscillating results are obtained only if an unreasonably low resolution is used and very few bins exist in the problematic radius range. However, in this case, the large droplet mode does not emerge and the moments are again far from the reference. Hence, our RMA implementation is not capable of producing reasonable results for the Long kernel.

It is not clear whether the oscillations are inherent to the original RMA algorithm or caused by the introduction of the reduction limiter. The latter might introduce discontinuities where instabilities could be triggered. The first option seems more probable, as the Golovin RMA simulations with Reduction limiter do not show any instability and gives a perfect agreement with the reference (see column 2 in Figs. 5 and 6). Similarly, Golovin RMA simulations with update on the fly are stable and close to the reference, however the results depend on the order in which the SIP combinations are processed (see column 3 (and 4) in Figs. 5 and 6). Again, Long simulations with an update on the fly version of RMA are unstable (not shown).

Andrejczuk et al. (2010) introduced and evaluated the RMA algorithm and applied it in a simulation of boundary layer stratocumulus. Our findings are seemingly in conflict with the conclusions of their evaluation exercises. What both studies have in common is a similar trend for a κ-variation. In

Geosci. Model Dev. Discuss., doi:10.5194/gmd-2016-271, 2016
Manuscript under review for journal Geosci. Model Dev.
Published: 28 November 2016

Geoscientific Model Development Discussions
Open Access
EGU

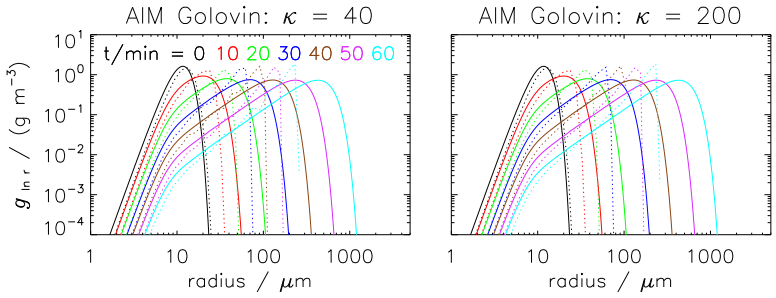

Figure 8. Mass density distributions obtained by the AIM algorithm for the Golovin kernel from $t = 0$ to $60\,\mathrm{min}$ every $10\,\mathrm{min}$ (from black to cyan). The solid curves show the reference solution, the dotted curves the simulation result of the AIM algorithm (ensemble average over 50 realisations). The parameter settings are: probabilistic singleSIP-init, $\nu_{critmin} = 10^{-9}\max(\nu_i)$, $\Delta t = 1\,\mathrm{s}$ and $\kappa = 40$ (left) or $\kappa = 200$ (right).

their Fig. 13, simulations for κ ranging roughly from 4 to 30 are depicted. The simulations with many bins show oscillations, whereas the coarsest simulation has no oscillations, but is clearly far from the real solution (largest droplets around $40\,\mu\mathrm{m}$ compared to $500\,\mu\mathrm{m}$ in the reference simulation). In their Fig. 14, they presented a detailed sensitivity test only for a $\kappa = 4$ simulation, which downplays the severity of the oscillation issue. Moreover, their simulations ran up to $2000\,\mathrm{s}$ compared to $3600\,\mathrm{s}$ in this study and many other studies (e.g. Bott, 1998; Wang et al., 2007). Hence, they missed the regime where the effect of the oscillations is strongest. Despite our extensive tests we cannot exclude that in Andrejczuk et al. (2010) an RMA implementation was used where oscillations are less cumbersome; however, the study missed to demonstrate this for a conclusive test case and we come to the conclusion that the evaluation exercises were incomplete and not suited to reveal the deficiencies faced here.

RMA simulations with the Hall kernel are similarly corrupted by oscillations and do not produce useful simulations either (not shown).

3.2 Performance of Average Impact (AIM) Algorithm

Fig. 8 displays DSDs obtained by AIM for the Golovin kernel. Compared to the reference, the droplets pile up at too small radii and the algorithm is not capable of reproducing the continuous shift to larger sizes, even if a fine grid with $\kappa = 200$ (right) instead of $\kappa = 40$ (left) is used. For both κ-values, the increase of the higher moments proceeds at a too low rate (see Fig. 9), whereas the decrease in droplet number matches the analytical evolution. AIM is a very robust algorithm in the sense that the results are fairly insensitive to most numerical parameters as demonstrated for κ and Δt in the left column of Fig. 9. Most simulations converge to—what we call—the best AIM solution, which is, however, not the same as the correct solution. The results deteriorate slightly if the initial

Geosci. Model Dev. Discuss., doi:10.5194/gmd-2016-271, 2016
Manuscript under review for journal Geosci. Model Dev.
Published: 28 November 2016

Geoscientific Model Development Discussions
Open Access
EGU

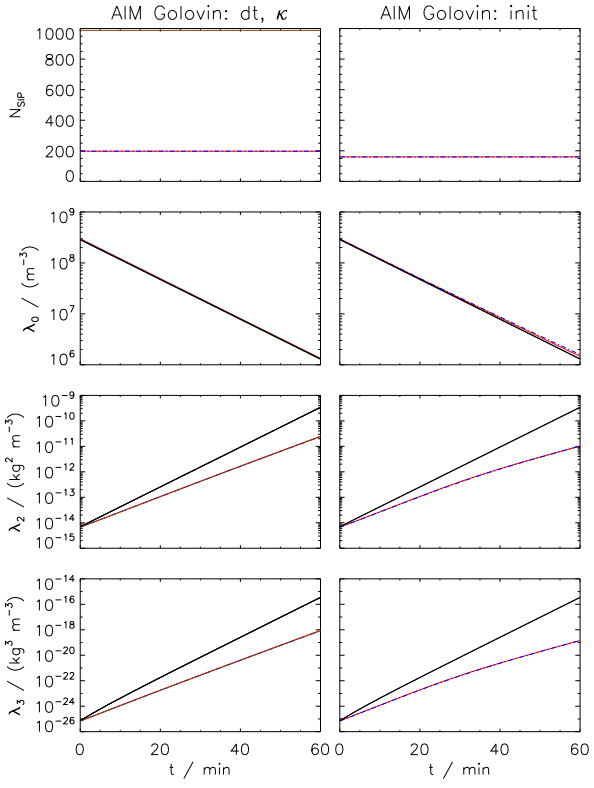

Figure 9. SIP number and moments λ_0, λ_2 and λ_3 as a function of time obtained by the AIM algorithm for the Golovin kernel. The black curves show the moments of the reference solution. All other curves depict the AIM results (average over 50 realisations). The default settings are: Probabilistic singleSIP-init, $\kappa = 40$, $\nu_{critmin} = 10^{-9} \max(\nu_i)$ and $\Delta t = 1\,\mathrm{s}$. Left column: default simulation (red), larger time step ($\Delta t = 10s$, blue) and more SIPs ($\kappa = 200$, brown). Right column: ν_{const}-init (red) and ν_{draw}-init (blue) with $N_{SIP} = 160$.

SIP ensemble is generated with the ν_{const}-init or ν_{draw}-init instead of with the singleSIP-init (right column of Fig. 9).

The algorithm performs, in general, better for the Long and Hall kernel as is detailed in the following. Fig. 10 displays DSDs obtained by AIM for the Long kernel. Generally, the results are in good agreement with the reference solution, as long as the SIP ensemble is initialised with the singleSIP-init method (left and middle column). Towards the end of the simulated period (magenta and cyan lines), the removal of small droplets is a bit underestimated and too many small droplets are present. For $t = 30$ and $40\,\mathrm{min}$, the large droplet mode is too weak as not enough large droplets have formed. At that stage, the droplets grow rapidly by collection and the AIM results lag behind. Although the offset is less than five minutes, it might become crucial in simulations of short-lived clouds. Also

Geosci. Model Dev. Discuss., doi:10.5194/gmd-2016-271, 2016
Manuscript under review for journal Geosci. Model Dev.
Published: 28 November 2016

Geoscientific Model Development Discussions
Open Access
EGU

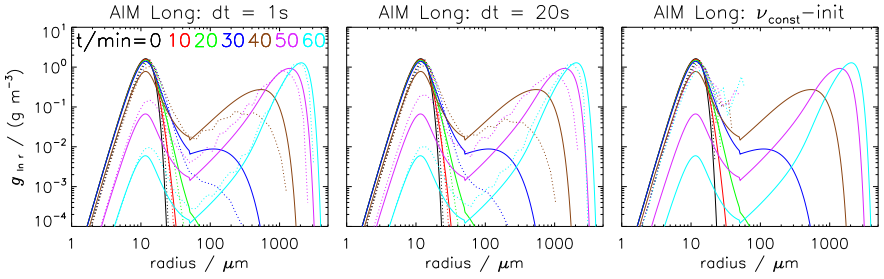

Figure 10. Mass density distributions obtained by the AIM algorithm for the Long kernel from $t = 0$ to $60\,\mathrm{min}$ every $10\,\mathrm{min}$ (from black to cyan). The solid curves show the reference solution, the dotted curves the simulation result of the AIM algorithm as an average over 50 realisations. The default settings are: Probabilistic singleSIP-init, $\kappa = 40$, $\nu_{critmin} = 10^{-9}\max(\nu_i)$, $\Delta t = 1\,\mathrm{s}$ (column 1); Δt increased to $20\,\mathrm{s}$ (column 2); ν_{const}-init technique with $N_{SIP} = 160$ (column 3).

the evolution of the moments (see Fig. 11) confirms this, as the onset of the rapid changes at around $t = 30\,\mathrm{min}$ is only slightly retarded if parameters are suitably chosen. Towards the end, the AIM results get again very close to the reference solution. The left column of Fig. 11 shows the dependence on the time step. For time steps $\Delta t \leq 20\,\mathrm{s}$ all results are similar to the best AIM solution which is close to the reference. Time steps of $50\,\mathrm{s}$ and more do not produce good enough results. Moreover, AIM is fairly insensitive to the choice of κ, $r_{critmin}$ and $\nu_{critmin}$ (see middle column). Simulations with κ ranging from 10 to 100 yield similar results. Only, for a very coarse resolution ($\kappa = 5$) with 25 SIPs, the decrease in droplet number is too small. Increasing the lower cutoff radius $r_{critmin}$ from $0.6\,\mu\mathrm{m}$ to $5\,\mu\mathrm{m}$, the $r < 5\,\mu\mathrm{m}$-part of the DSD is represented by a single SIP and N_{SIP} is reduced by 60%. The predicted moments are unaffected by this variation. Those small-r_i SIPs are not relevant for the AIM performance. They simply carry too small fractions of the total grid box mass to be important. Their status will not change over time as already illustrated in Fig. 3. Similarly, a variation of $\nu_{critmin}$ or the switch to a strict threshold $\nu_{critmin}$ has no effect.

Now we draw the attention to the importance of the SIP-init method. The right panel of Fig. 10 shows the DSDs when the SIPs are initialised with the ν_{const}-init method. The algorithm completely fails and no droplets larger than $70\,\mu\mathrm{m}$ occur after 60 minutes. Consequently, the moments are far off from the reference solution (solid lines in the right column of Fig. 11). Switching to the ν_{draw}-init method (dotted lines) or using many more SIPs (up to 1600) improves the results, yet they are still useless. This clearly demonstrates how crucial the initial characteristics of the SIP ensemble are. Initialising the SIPs with an appropriate technique like the singleSIP-init, useful results are obtained with as few as 50 SIPs. Using the ν_{const}-init or ν_{draw}-init, on the other hand, solutions are still useless, even though the number of SIPs and the computation time are factor 30 and 900 higher.

Geosci. Model Dev. Discuss., doi:10.5194/gmd-2016-271, 2016
Manuscript under review for journal Geosci. Model Dev.
Published: 28 November 2016

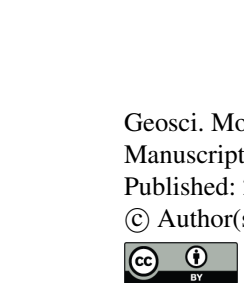

Geoscientific Model Development Discussions
Open Access
EGU

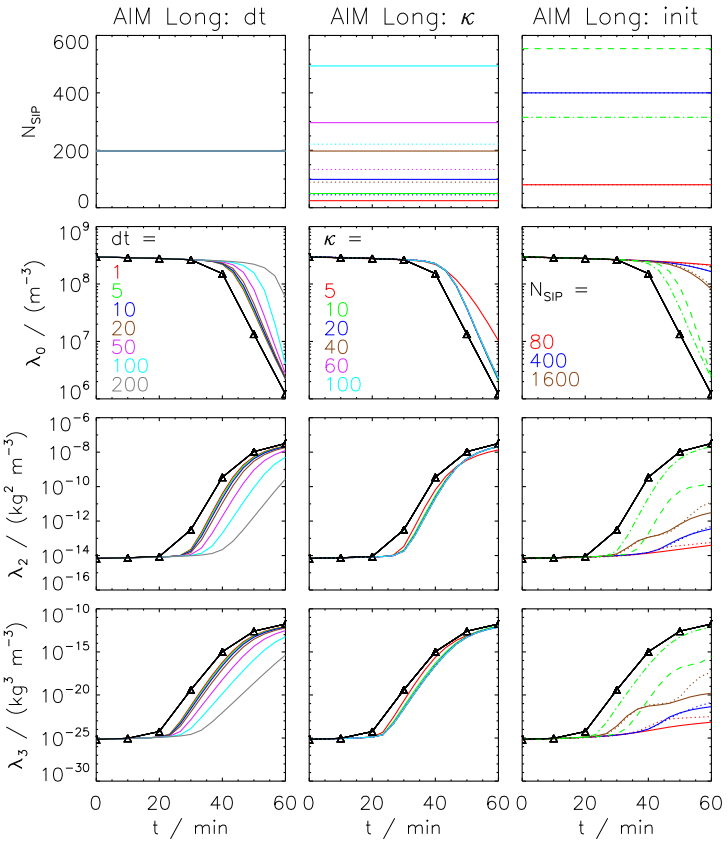

Figure 11. SIP number and moments λ_0, λ_2 and λ_3 as a function of time obtained by the AIM algorithm for the Long kernel. The black curves show the moments of the reference solution. All other curves depict the AIM results (average over 50 realisations). The left column shows a variation of $\Delta t = 1,\ 5,\ 10,\ 20,\ 50,\ 100,\ 200\,\mathrm{s}$ for $\kappa = 40$. The middle column a variation of $\kappa = 5,\ 10,\ 20,\ 40,\ 60,\ 100$ for $\Delta t = 10\,\mathrm{s}$. Either, the default singleSIP-init (solid) or the singleSIP-init with $r_{critmin} = 5\,\mu\mathrm{m}$ (dotted) is used. The right column displays simulations with different initialisation techniques and $\Delta t = 10\,\mathrm{s}$: the ν_{const}-init (solid) and ν_{draw}-init (dotted) with $N_{SIP} = 1600,\ 400,\ 80$ as well as the $\nu_{random,rs}$-init (dashed) and $\nu_{random,lb}$-init (dash-dotted) with $(\alpha_{high}, \alpha_{med}, \alpha_{low}) = (10^{-2},\ 10^{-3},\ 10^{-13})$ and threshold radius $r_{lb} = 16\,\mu\mathrm{m}$.

Geosci. Model Dev. Discuss., doi:10.5194/gmd-2016-271, 2016
Manuscript under review for journal Geosci. Model Dev.
Published: 28 November 2016

Geoscientific Model Development Discussions
Open Access
EGU

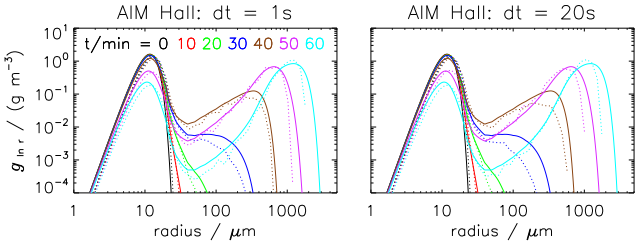

Figure 12. Mass density distributions obtained by the AIM algorithm for the Hall kernel from $t = 0$ to $60\,\mathrm{min}$ every $10\,\mathrm{min}$ (from black to cyan). The solid curves show the reference solution, the dotted curves the simulation result of the AIM algorithm as an average over 50 realisations. The default settings are: Probabilistic singleSIP-init, $\kappa = 40$, $\nu_{critmin} = 10^{-9}\max(\nu_i)$, $\Delta t = 1\,\mathrm{s}$ (column 1); Δt increased to $20\,\mathrm{s}$ (column 2).

The ν_{random}-simulations give another example of the importance of the init method. Even though both techniques, $\nu_{random,rs}$ (dashed line) and $\nu_{random,lb}$ (dash-dotted line), are similar in design and differ only in the creation of the largest SIPs (see Fig. 1), the outcome of the simulations is quite different. For the $\nu_{random,lb}$-init, the solution matches the best AIM solution, whereas for $\nu_{random,rs}$ the moments λ_2 and λ_3 stagnate at too low levels. The latter test pinpoints the main weakness of the AIM which is also reflected in its name (average impact). The initial weighting factors of those SIPs (in relation to ν of the remaining SIPs) controls how strong this growth is and how the large droplet mode emerges.

All quantities shown in Fig. 9 and 11 are averages over 50 realisations of the initial SIP ensemble. All individual realisations yield basically identical simulation results and it would have been sufficient to carry out and display simulations of a single realisation.

Figure 12 shows DSDs of simulations with the Hall kernel. Compared to the Long simulations, small droplets are much more abundant (see reference solution), as the collection of small droplets proceeds at a lower rate. This makes the simulation less challenging from a numerical point of view and AIM DSDs come closer to the reference than in the Long simulations. Consequently, the AIM moments agree very well with the reference as shown in Fig. 13. For $\Delta t \leq 20\,\mathrm{s}$ and $\kappa \geq 20$, all solutions are similar to the best AIM solution.

3.3 Performance of All-Or-Nothing (AON) Algorithm

Fig. 14 shows the AON results for the Golovin kernel. An excellent agreement with the reference solution is found which proves at least the correct implementation of AON. Switching to a version without multiple collections (i.e. SIP i collects at most ν_i droplets in every time step) does not affect the solution as cases with $p_{crit} > 1 \Leftrightarrow \nu_k > \nu_i$ occur rarely. The AON moments closely follow the reference solution, even when the time step is increased from $1\,\mathrm{s}$ to $10\,\mathrm{s}$ or fewer SIPs are used when κ is decreased from 40 to 10 (left column of Fig. 15). Unlike to AIM, AON is successful, even when

Geosci. Model Dev. Discuss., doi:10.5194/gmd-2016-271, 2016
Manuscript under review for journal Geosci. Model Dev.
Published: 28 November 2016

Geoscientific Model Development Discussions
Open Access
EGU

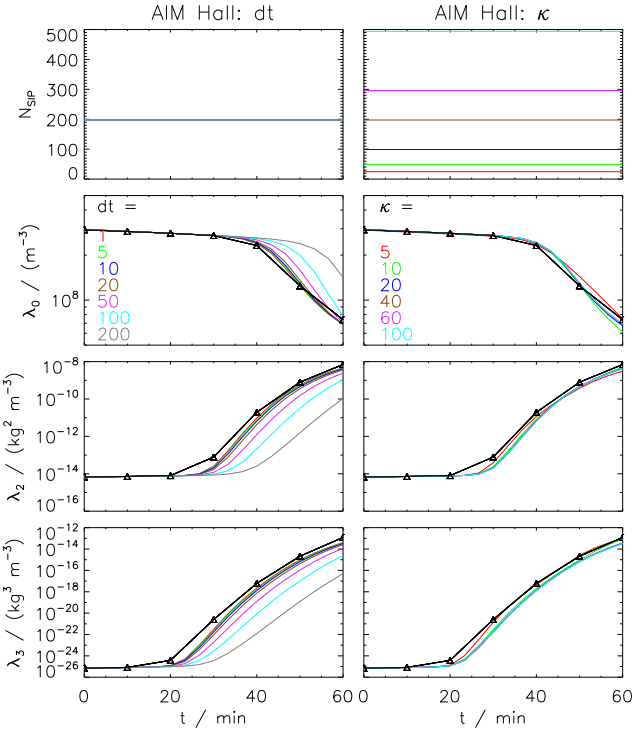

Figure 13. SIP number and moments λ_0, λ_2 and λ_3 as a function of time obtained by the AIM algorithm for the Hall kernel. The black curves show the moments of the reference solution. All other curves depict the AIM results (average over 50 realisations). The left column shows a variation of $\Delta t = 1,\ 5,\ 10,\ 20,\ 50,\ 100,\ 200\,\mathrm{s}$ for $\kappa = 40$ and the right column a variation of $\kappa = 5,\ 10,\ 20,\ 40,\ 60,\ 100$ for $\Delta t = 10\,\mathrm{s}$

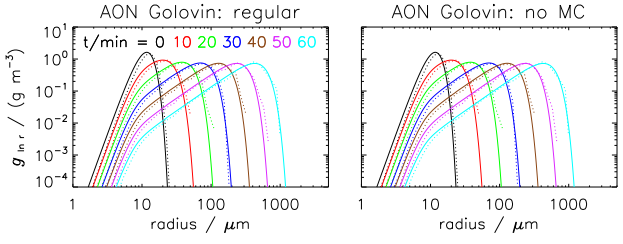

Figure 14. Mass density distributions obtained by the AON algorithm for the Golovin kernel from $t = 0$ to $60\,\mathrm{min}$ every $10\,\mathrm{min}$ (from black to cyan). The solid curves show the reference solution, the dotted curves the simulation result of the AON algorithm (ensemble average over 50 realisations). The parameter settings are: probabilistic singleSIP-init, $\kappa = 40$, $\nu_{critmin} = 10^{-9}\max(\nu_i)$, $\Delta t = 1\,\mathrm{s}$. The columns show various variants of the algorithm: default version, version disregarding multiple collections and version disregarding self-collections (from left to right).

Geosci. Model Dev. Discuss., doi:10.5194/gmd-2016-271, 2016
Manuscript under review for journal Geosci. Model Dev.
Published: 28 November 2016

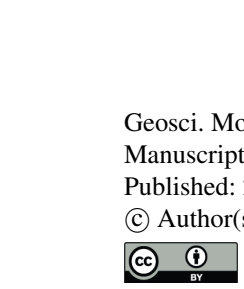

Geoscientific Model Development Discussions
Open Access
EGU

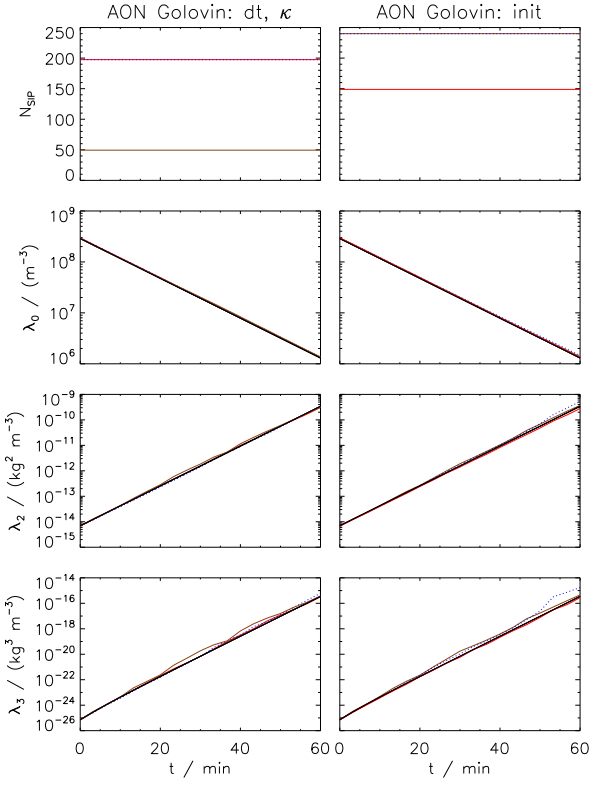

Figure 15. SIP number and moments λ_0, λ_2 and λ_3 as a function of time obtained by the AON algorithm for the Golovin kernel. The black curves show the moments of the reference solution. All other curves depict the AON results (average over 50 realisations). The default settings are: Probabilistic singleSIP-init, $\kappa = 40, \nu_{critmin} = 10^{-9} \max(\nu_i)$ and $\Delta t = 1\,\mathrm{s}$. Left column: default simulation (red), larger time step ($\Delta t = 20s$, blue) and fewer SIPs ($\kappa = 10$, brown). Right column: ν_{const}-init (brown) , ν_{draw}-init (blue) and singleSIP-init with $r_{critmin} = 1.6\,\mu\mathrm{m}$ (red).

Geosci. Model Dev. Discuss., doi:10.5194/gmd-2016-271, 2016
Manuscript under review for journal Geosci. Model Dev.
Published: 28 November 2016

Geoscientific Model Development Discussions
Open Access
EGU

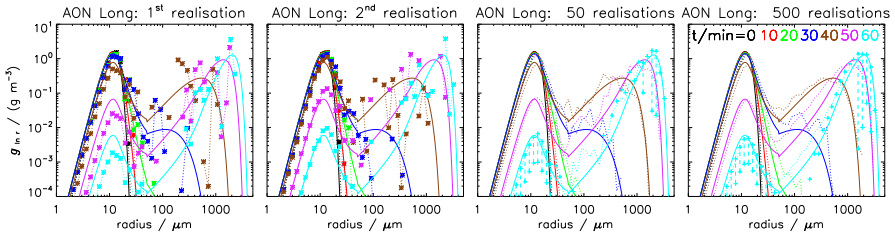

Figure 16. Mass density distributions obtained by the AON algorithm for the Long kernel from $t = 0$ to $60\,\mathrm{min}$ every $10\,\mathrm{min}$ (from black to cyan). The solid curves show the reference solution, the dotted curves the simulation result of the AON algorithm. Columns 1 and 2 show individual realisations (each $*$-symbol depict a non-zero g-value). Columns 3 and 4 show averages over 50 and 500 realisations. For each bin, the interquartile range is determined and depicted by $+$-symbols with a dashed bar (only for $t = 60\,\mathrm{min}$). If there is only one $+$-symbol, the 25th percentile is too small to be visible. The settings are: Probabilistic singleSIP-init, $\kappa = 40$, $\nu_{critmin} = 10^{-9}\max(\nu_i)$, $\Delta t = 20\,\mathrm{s}$.

the initial SIP ensemble is created with the ν_{const}-init or ν_{draw}-init (right column of Fig. 15). The moments are averages over 50 realisations. For the ν_{draw}-init method, the deviation in λ_3 towards the end of the simulated period is due to a single outlier realisation where the initial values of the moments λ_2 and λ_3 were already much higher than λ_2 and λ_3 of the reference solution. Column 2 of Fig. 1 already illustrated the large uncertainty of the initial values, which becomes increasingly larger for higher order moments. Hence, this outlier behaviour is associated with a deficiency of the init technique rather than being an algorithm-intrinsic feature.

Nevertheless, the simulations reveal large differences between individual realisations which deserves a closer inspection. Fig. 16 displays DSDs of AON for the Long kernel. The two left panels show DSDs of single realisations. The $*$-symbol depicts the g-value for each bin. Those symbols are connected by default. An interruption of the connecting line indicates one or more empty bins ($g = 0$) where no SIPs exist in this specific radius interval. This occurs frequently and the solutions are full of spikes and irregularly over- and undershoot the reference solution, particularly in the large droplet mode. The small droplet mode is underestimated in the first realisation and overestimated in the second realisation. The advantages of AON become apparent when the DSDs are averaged over many realisations as shown in columns 3 and 4. Then the DSDs come close to the reference solution and the interquartile range indicates the broad envelope the individual realisations span around the reference solution. Whereas the average over 50 realisations still has some fluctuations, the average over 500 realisations produces a smooth solution. There are two sources that are potentially responsible for the large ensemble spread: the probabilistic SIP initialisation and the probabilistic AON approach. In a sensitivity test, 50 realisations are computed, all using the same SIP initialisation obtained by a deterministic singleSIPinit. Figure 17 compares those simulations to regular simulations

Geosci. Model Dev. Discuss., doi:10.5194/gmd-2016-271, 2016
Manuscript under review for journal Geosci. Model Dev.
Published: 28 November 2016

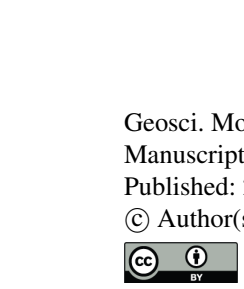

Geoscientific Model Development Discussions
Open Access
EGU

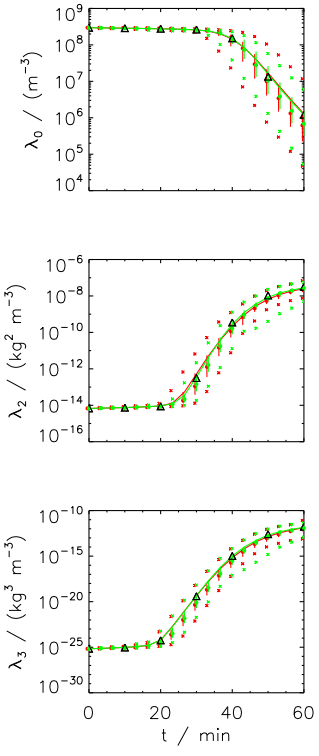

Figure 17. Moments λ_0, λ_2 and λ_3 as a function of time obtained by the AON algorithm for the Long kernel. Each realisation was initialised with a different SIP ensemble (probabilistic singleSIP, red) or all realisations started with the same SIP ensemble (deterministic singleSIP, green). In both cases, the curves show an average over 50 realisations with the vertical bars indicating the interquartile range. The crosses show the minimum and maximum values and the circle the median value. The black symbols depict the reference solution. The parameter settings are $\Delta t = 20$ and $\kappa = 40$.

Geosci. Model Dev. Discuss., doi:10.5194/gmd-2016-271, 2016
Manuscript under review for journal Geosci. Model Dev.
Published: 28 November 2016

Geoscientific Model Development Discussions
Open Access
EGU

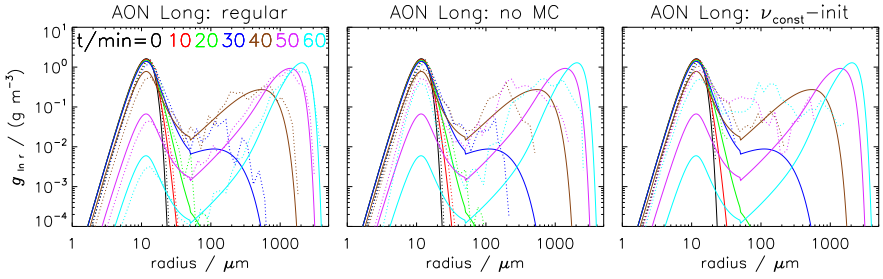

Figure 18. Mass density distributions obtained by the AON algorithm for the Long kernel from $t = 0$ to 60 min every 10 min (from black to cyan). The solid curves show the reference solution, the dotted curves the simulation result of the AON algorithm as an average over 50 realisations. The default settings are: Probabilistic singleSIP-init, $\kappa = 40$, $\nu_{critmin} = 10^{-9} \max(\nu_i)$, $\Delta t = 1$ s (column 1); version disregarding multiple collections at $\Delta t = 10$ s (column 2); ν_{const}-init technique with $N_{SIP} = 160$ (column 3).

with differing SIP initialisations. In both cases, we find a substantial ensemble spread. Starting with identical SIP initialisations the spread is, however, smaller suggesting that both sources contribute to the ensemble spread.

Fig. 18 shows AON results with 50 realisations and probabilistic initialisation which gives a good trade-off between computational cost and representativeness. Clearly, AON DSDs are less smooth than those of AIM. Column 1 shows a default simulation with singleSIP init and shows very good agreement with the reference solution. Disenabling multiple collections (column 2), far too few small droplets become collected and their abundance is substantially overestimated. As a consequence, the mass transfer from small to large droplets is slowed down and the large droplet mode is underestimated. Using the ν_{const}-init, the large droplet mode is not well matched and results are again useless. Fig. 19 shows the temporal evolution of moments λ_0, λ_2 and λ_3 for a large variety of sensitivity tests. Column 1 shows a variation of Δt for the singleSIP-init. The larger Δt is chosen, the more often combinations with $p_{crit} > 1$ occur and the more crucial it becomes to consider multiple collections. Even for the smallest time step considered, the version without multiple collections does not collect enough small droplets and hence overestimates droplet number. With the regular AON version considering multiple collections, reasonable results are obtained for time steps $\Delta t \leq 20$ s. Column 2 shows a variation of κ for singleSIP-init. Whereas the higher moments perfectly match the reference, the droplet number shows a non-negligible dependence on κ. For $\kappa < 100$, droplet number decrease is faster, the finer the resolution is. For $\kappa > 100$, a variation of κ has no effect, hence convergence is reached. However, those simulations underestimate the droplet number. Best results are obtained for an intermediate resolution of $\kappa = 40$. Using the MultiSIP-init, the simulations show the same undesired behaviour. Hence, increasing the SIP concentration in the middle part of the initial DSD has no positive effect despite using around 160% more SIPs. In another experiment, the hybrid singleSIP-

Geosci. Model Dev. Discuss., doi:10.5194/gmd-2016-271, 2016
Manuscript under review for journal Geosci. Model Dev.
Published: 28 November 2016

Geoscientific Model Development Discussions
Open Access
EGU

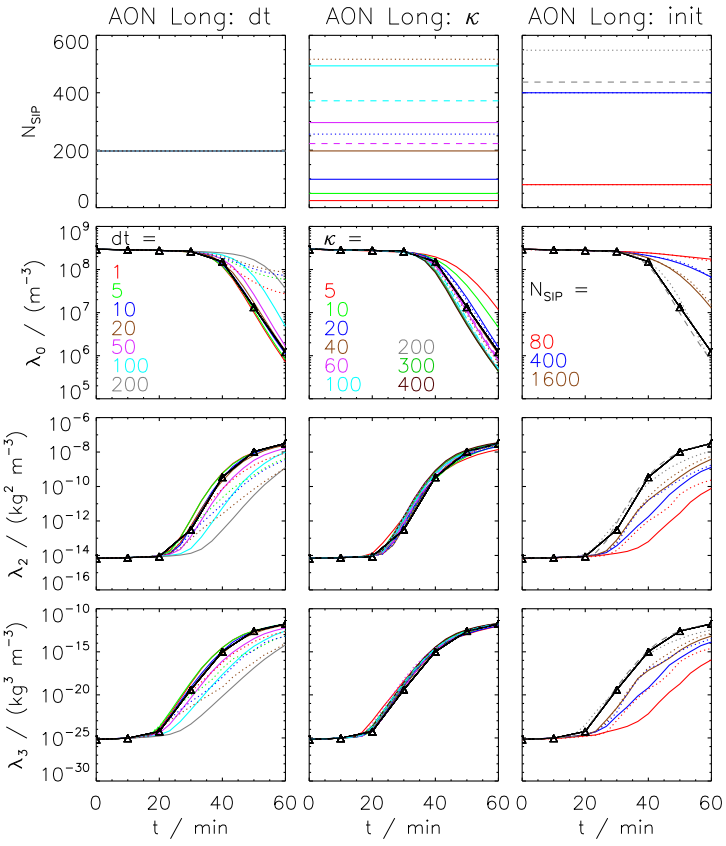

Figure 19. SIP number and moments λ_0, λ_2 and λ_3 as a function of time obtained by the AON algorithm for the Long kernel. The black symbols depict the moments of the reference solution. All coloured curves show the AON results (average over 50 realisations). The left column shows a variation of $\Delta t =$ 1, 5, 10, 20, 50, 100, 200 s for $\kappa = 40$ for the regular AON version (solid) and for a version disregarding multiple collections (dotted, only cases with $\Delta t \leq 20$ s are displayed). The middle column shows a variation of $\kappa =$ 5, 10, 20, 40, 60, 100, 200, 300, 400 for singleSIP-init (solid), singleSIP-init with $r_{critmin} = 1.6\,\mu$m (dashed, only for $\kappa = 60$ and 100) and MultiSIP-init (dotted, only for $20 \leq \kappa \leq 100$). The right column shows simulations with the ν_{const}-init (solid) and ν_{draw}-init (dotted) with $N_{SIP} =$ 1600, 400, 80. The gray dashed and dotted line show simulations with $\nu_{random,lb}$-init and $\nu_{random,rs}$-init, respectively. All simulations shown in the middle and right panel use $\Delta t = 10$ s.

Geosci. Model Dev. Discuss., doi:10.5194/gmd-2016-271, 2016
Manuscript under review for journal Geosci. Model Dev.
Published: 28 November 2016

Geoscientific Model Development Discussions
Open Access
EGU

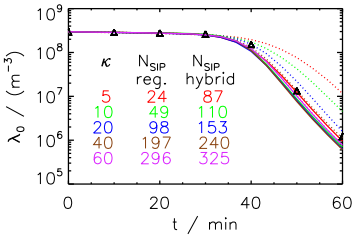

Figure 20. Droplet number as a function of time obtained by the AON algorithm for the Long kernel. The black symbols show the moments of the reference solution. The solid/dotted curves show simulations with hybrid/regular singleSIP-init for various κ-values (5 to 60, see legend). The hybrid version uses $\kappa = 100$ for radii above $15\,\mu$m and κ as labeled for radii below $15\,\mu$m. The hybrid version uses more SIPs than the regular version (see N_{SIP}-values listed in the plot). The dotted lines are identical to solid lines in col 2 of 19

init was used. Below $r = 16\,\mu$m SIPs are initialised as usually. Above this radius, a high resolution with $\kappa = 100$ is always used irrespective of the chosen κ. Clearly, more SIPs are initialised with this hybrid version relative to the original version (see N_{SIP}-values listed in the figure legend). Figure 20 shows the droplet number evolution for the original singleSIP-init and the new hybrid version. The sensitivity to κ is basically suppressed when the hybrid version is used. This implies that the AON algorithm is more or less insensitive to the resolution in radius range $r < 16\,\mu$m, however, it is sensitive to the SIP resolution in the right tail. For example, the $\kappa = 5$-simulation with the hybrid version and 87 SIPs performs better than the $\kappa = 20$-simulation with the regular init and 98 SIPs.

In the conventional version, SIPs are initialised down to a radius of $0.6\,\mu$m (as can be seen in the top left panel of Fig. 1). Another variation of the singleSIP-init is shown in column 2 of Fig. 19 (dashed curves) where this lower cut-off radius is raised to $1.6\,\mu$m and around $25\,\%$ fewer SIPs are used to describe the DSD. The simulation results are basically identical to the conventional init version and suggest that those initially small-r_i, small-ν_i SIPs are not relevant for the performance of AON.

Further tests with the singleSIP-init include a variation of the threshold parameter η and a switch from weak thresholds to strict thresholds. Moreover, we investigated the implications of update-on-the-fly of the SIP properties. The singleSIP-init produces an initially radius-sorted SIP ensemble and looping over the i-j combinations in the algorithm starts with combinations of the smallest droplets, which may introduce a bias. We reversed the order (i.e. started with largest droplet combinations) or randomly rearranged the order of the SIP combinations. None of those variations had a significant effect on the results (not shown).

Finally, the AON performance for other SIP initialisations is discussed (right column of Fig. 19). As already demonstrated in Fig. 18, AON is not able to produce a realistic large droplet mode, if a moderate number of SIPs is initialised with the ν_{const}-technique. Hence, the higher moments are

Geosci. Model Dev. Discuss., doi:10.5194/gmd-2016-271, 2016
Manuscript under review for journal Geosci. Model Dev.
Published: 28 November 2016

underestimated and droplet number is overestimated. Increasing the number of SIPs up to 1600, the solutions get closer to the reference, yet the agreement is still not satisfactory. The performance for the ν_{draw}-init is similar. Keeping in mind the previous sensitivity studies (hybrid singleSIP-init, MultiSIP-init), it is apparent that the ν_{const}-init and ν_{draw}-init suffer from an undersampling of the initially largest droplets. Due to its simplicity, using constant weights for initialisation has been a common approach in previous 3D-LCM cloud simulations (Shima et al., 2009; Hoffmann et al., 2015). Hence, we tested AON extensions aiming at a better performance for equal weights initialisations. Let us consider the possible weighting factors the SIPs can attain in the course of a simulation. In the beginning, all SIPs have $\nu = \nu_{init}$. After a collection event, for both involved SIPs $\nu = \nu_{init}/2$. If such a $\nu = \nu_{init}/2$-SIP collects a $\nu = \nu_{init}$-SIP, both SIPs carry $\nu_{init}/2$ droplets. Subsequent collections can generate SIPs with weighting factors $\nu_{init}/4$, $3\,\nu_{init}/4$ and so on. It may be advantageous, if AON generates a broader spectrum of possible ν-values and produces SIPs with smaller weights more efficiently. So far, the equal splitting approach with $\xi = 0.5$ in a collection event of two equal-ν SIPs has been used. In sensitivity tests, a random number for ξ is drawn in each collection event, either from a uniform distribution $\xi \in [0,1]$ or from a log-uniform distribution $\xi \in [10^{-10}, 10^{0}]$. Enhancing the spread of ν-values, more collection events occur in the algorithm, as p_{crit} is smaller when small-ν SIPs are involved. Once most SIPs were part of a collection event, the first option with $\xi \in [0,1]$ produces a distribution of ν-values that is similar to the initial ν-distribution of the ν_{draw}-init technique. Hence, the new version does not improve the simulation results, as the outcome for the ν_{draw}-init and the standard ν_{const}-init are similar (not shown). Other variations produce smaller weights with $\xi = 10^{-10\ rand()}$ or $\xi = 10^{-10\ rand()^2}$, yet without any noticeable improvement in the simulation results (not shown).

To complete the analysis for the Long kernel, the right column of Fig. 19 shows simulation results for $\nu_{random,lb}$ and $\nu_{random,rs}$. In short, AON can cope with those initialisations and produces useful results.

As already noted in the AIM section, Hall simulations are not as challenging as Long simulations from a numerical point of view. As the collection of small droplets proceeds at a lower rate for the Hall kernel, disenabling multiple collections in the AON simulations does not deteriorate the results as much as in the Long simulations (not shown). Besides this, simulations with the Hall kernel lead to similar conclusions as for the Long simulations and are therefore not discussed in more detail.

4 Discussion

The presented box model simulations can be regarded as a first evaluation step of collection/aggregation algorithms in LCMs. The final goal is the evaluation in (multi-dimensional) applications of LCMs with full microphysics. In order to isolate the effect of collection, other microphysical processes like droplet formation and diffusional droplet growth have been switched off and all box model simula-

Geosci. Model Dev. Discuss., doi:10.5194/gmd-2016-271, 2016
Manuscript under review for journal Geosci. Model Dev.
Published: 28 November 2016

tions started with a prescribed SIP ensemble following a specific exponential distribution. The evaluation of different initialisation methods showed that the performance of the collection/aggregation approaches depends essentially on the way the SIPs are initialised, a problem which is inherently absent in spectral-bin models. Their initialisation resembles the singleSIP technique used here, i.e. the number concentration (the weighting factor) within a bin (for a certain mass range represented by one SIP) is directly prescribed. However, LCMs exhibit a larger variety of how an initial droplet spectrum can be translated into the SIP space. The study showed that the singleSIP is advantageous for the correct representation of the collisional growth, since they initialise large SIPs with small weighting factors, which are responsible for the strongest radius growth. On the other hand, the ν_{const} initialisation technique, in which all SIPs have the same weighting factor initially as it is done in many current (multi-dimensional) applications of LCMs, impedes significantly the correct representation of collisional growth.

In this idealised study, we were able to control (to a certain extent) the representation of droplet spectra by various initialisation methods. In more-dimensional simulations with full microphysics, however, this is not straightforward nor has it been intended. So far, convergence tests in "real-world" LCM applications simply included variations of the SIP number and have not focused on more detailed characteristics of the SIP ensemble (i.e. the properties that have been discussed in Fig. 1). Droplet formation and diffusional droplet growth, which usually create the spectrum from which collisions are triggered, should be implemented such that "good" SIP ensembles are generated or evolve before collection becomes important. Here, good refers to a SIP ensemble for which the collection/aggregation algorithm performs well. For instance, the basic idea of the initialisation technique ν_{random}, the initialisation of weighting factors uniformly distributed in $\log(\nu)$, might also improve multi-dimensional simulations.

Generally, the performance of the algorithms is better when the SIP ensemble features a broad range of weighting factors. One viable option to achieve this is the introduction of a SIP splitting technique (Unterstrasser and Sölch, 2014). Why this may improve the performance of the collection/aggregation algorithms is outlined next. Mass fractions represented by individual SIPs, $\tilde{\chi}_i$, are analysed. $\tilde{\chi}_i$ is defined as $\chi_i/\mathcal{M}$, i.e. the total droplet mass in a SIP χ_i is normalised by the total mass within the grid box $\mathcal{M}$. Figure 21 shows the initial $\tilde{\chi}_i$-values for the singleSIP-init method and two resolutions $\kappa = 20$ and 100 as a function of their initial radius r_i. The two rows show the same data, using a logarithmic (top row) or linear y-scale (bottom). The log scale version highlights that $\tilde{\chi}_i$-values spread over many orders of magnitudes. Mainly, the parameter $\nu_{critmin}$ controls the minimum value of χ_i. The heaviest SIPs carry initially up to 6.5% ($\kappa = 20$) or 1.2% ($\kappa = 100$) of the total mass $\mathcal{M}$ (see bottom row). Clearly, the values of the $\kappa = 20$-simulation are larger, as the total mass is distributed over fewer SIPs. For each SIP, $\tilde{\chi}_i$ is tracked over time and the maximum value, $\tilde{\chi}_{i,max(t)}$, is recorded (red and brown curves in the graphs). Characteristically of AIM, only the largest SIPs grow substantially and collect mass from other SIPs. Hence, only χ_i of those SIPs

Geosci. Model Dev. Discuss., doi:10.5194/gmd-2016-271, 2016
Manuscript under review for journal Geosci. Model Dev.
Published: 28 November 2016

Geoscientific Model Development Discussions
Open Access
EGU

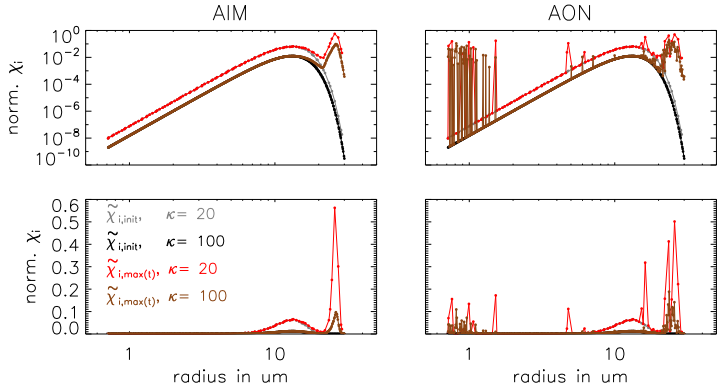

Figure 21. Normalised SIP mass $\tilde{\chi}_i$ as a function of the initial SIP radius r_i. $\tilde{\chi}_i$ is defined as $= \chi_i/\mathcal{M} = (\nu_i \mu_i)/\mathcal{M}$, i.e. the total droplet mass in a SIP is normalised by the total mass within the grid box. χ_{init} denotes $\tilde{\chi}_i$ of the initial SIP ensemble. χ_{max} denotes the maximum $\tilde{\chi}_i$-value each SIP attains over the course of a simulation. The left/right panel shows AIM/AON simulations with $\kappa = 20$ or 100 (see legend). singleSIP-init, $\Delta t = 10\,\mathrm{s}$.

increases. By the way, this also illustrates that the χ_i-values of the smallest SIPs are so small that all those SIPs can be merged into a single SIP without changing the AIM outcome (see $r_{critmin}$-variation before). Using the fine resolution ($\kappa = 100$), heavy SIPs carry up to 10% of the total grid box mass at some point in time. In the $\kappa = 20$-simulation, this ratio can be higher than 50%, meaning that one specific SIP accumulated more than 50% of the total grid box mass at some time. Hence, the grid box mass is distributed fairly unevenly over the SIP ensemble. Astonishingly, this has no effect on the performance of AIM as the predicted $\lambda_{k,SIP}$-values for both AIM simulations are basically identical (see middle column of Fig. 11). In the AON simulations, we similarly find that the grid box mass is unevenly distributed over the SIP ensemble. Different to AIM, also many initially small SIPs and a few initially medium-sized SIPs carry a relevant portion of the grid box mass at some time. The algorithms may converge better if those heavy SIPs are split into several SIPs during the simulation.

In all simulations so far, the mean radius of the initial DSD was $9.3\,\mu\mathrm{m}$ where the abundance of droplets larger than $10\,\mu\mathrm{m}$ drops strongly, which poses a challenge to the representation in SIP space. In a sensitivity test, we start with "more mature" DSDs. The simulations are initialised with Wang's reference solution after $t_{init} = 10$, 20 or 30 minutes (cf. red, green and blue solid curves in previous plots of mass density distributions) using the singleSIP-init. Fig. 22 shows the SIP number and various moments of the DSD for AIM and AON. The initial DSD is broader for a later initialisation time and hence more SIPs are initialised for a given κ. This implies in particular that the spectrum above $10-20\,\mu\mathrm{m}$ is sampled with more SIPs. For both algorithms, the simulation results are close to the reference solution. Compared to the default $t_{init} = 0$-case, a much weaker κ-dependence of the

Geosci. Model Dev. Discuss., doi:10.5194/gmd-2016-271, 2016
Manuscript under review for journal Geosci. Model Dev.
Published: 28 November 2016

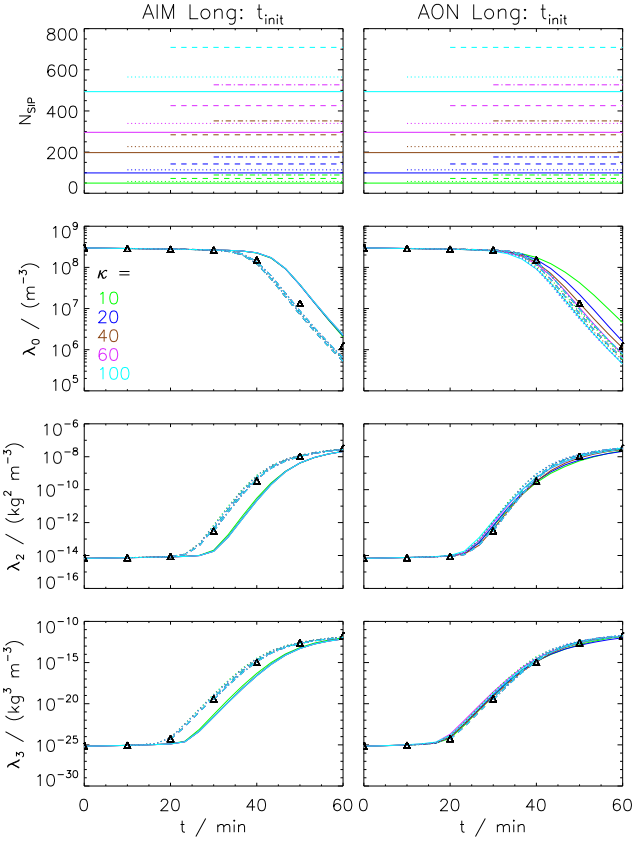

Figure 22. SIP number and moments λ_0, λ_2 and λ_3 as a function of time obtained for the Long kernel by AIM (left) and AON (right). The black symbols depict the moments of the reference solution. The simulations are initialised with Wang solution after 10 (dotted), 20 (dashed) or 30 (dash-dotted) minutes using the singleSIP-init with various κ-values (see legend). The default AON and AIM simulations initialised at $t = 0$, which have been shown before in Figs. 11 and 19, are depicted by solid lines.

Geosci. Model Dev. Discuss., doi:10.5194/gmd-2016-271, 2016
Manuscript under review for journal Geosci. Model Dev.
Published: 28 November 2016

AON predicted droplet number is apparent and the AIM results do not lag behind. Even though this sensitivity test cannot be repeated for other init methods (as they require an analytical description of the initial DSD), the singleSIP simulations already indicate that the SIP initialisation is not as crucial when a later initialisation time is chosen and that our default setup with a narrow DSD may overrate the importance of the SIP initialisation. What are the implications of this for simulations with full microphysics? Clearly, the $t_{init} = 20\,\mathrm{min}$ and $30\,\mathrm{min}$-case oversimplify the problem, as such DSDs cannot be produced by diffusional growth only. The $t_{init} = 10\,\mathrm{min}$-DSD, on the other hand, is still close to the $t_{init} = 0\,\mathrm{min}$-DSD and may be produced by diffusional growth.

In multi-dimensional models, collection/aggregation might be further influenced by the movement of SIPs due to sedimentation or flow dynamics. For instance, sedimentation removes the largest SIPs with the smallest weighting factors, while turbulent mixing is able to add SIPs with their initial weighting factor into matured grid boxes, where collection has already decreased the weighting factors of the older SIPs. Indeed, the additional variability in more-dimensional simulations might compensate for the missing variability in the weighting factors usually present in simulations using the ν_{const} initialisation technique.

It is not clear which findings of our evaluation efforts are the most relevant aspects that control the performance of collection/aggregation algorithms in more complex LCM simulations. Nevertheless, the idealised box simulations are an essential prerequisite towards more comprehensive evaluations as they disclosed the potential importance of the SIP initialisation (an aspect that is inherently absent in spectral bin models). All in all, we can state that the behaviour of Lagrangian collection algorithms in more complex simulations demands further investigation. Nevertheless, we have already learned a lot from the box model simulations. A summary will be given in the concluding section.

Besides the academic Golovin kernel, our simulations used the hydrodynamic kernel with collection efficiencies that are usually employed for liquid clouds (Long and Hall). We found that Hall simulations are not as challenging as Long simulations from a numerical point of view. For ice clouds, usually a constant aggregation efficiency E_a (the analogon to collection efficiency) is chosen, partly due to the lack of better estimates (Connolly et al., 2012). AON simulations with $E_a = 0.2$ indicated that using a constant efficiency makes the computational problem less challenging, e.g. we find a smaller sensitivity to κ compared to the Long simulations shown in Fig. 19 (not shown). Hence, the presented algorithms can be equally employed for aggregation. Certainly, the assumption of spherical particles used here is overly simplistic for ice cloud, in particular, if aggregates form. However, including mass-area relationships (e.g. Mitchell, 1996; Schmitt and Heymsfield, 2010) in the kernel expression and using parameterisations of ice crystal fall speed (e.g. Heymsfield and Westbrook, 2010) should not change the nature of the problem.

Geosci. Model Dev. Discuss., doi:10.5194/gmd-2016-271, 2016
Manuscript under review for journal Geosci. Model Dev.
Published: 28 November 2016

Geoscientific Model Development Discussions
Open Access
EGU

5 Conclusions

In the recent past, Lagrangian cloud models (LCMs), which use a large number of simulation particles (SIPs) to represent a cloud, have been developed and become more and more popular. Each SIP represents a certain number of real droplets, which is termed the weighting factor of a SIP. In particular, the collision process leading to coalescence of cloud droplets or aggregation of ice crystals is implemented differently in the various models described in the literature. The present study evaluates the performance of three different collection algorithms in a box model framework. All microphysical processes except collection/aggregation are neglected and an exponential droplet mass distribution is used for initialisation. The box model simulation results are compared to analytical solutions (in the case of the Golovin kernel) and to a reference solution obtained from a spectral bin model approach by Wang et al. (2007) (in the case of the Long or Hall kernel).

LCMs exhibit a large variety of how an initial droplet spectrum can be translated into the SIP space and various initialisation methods are thoroughly explained. The performance of the algorithms depends crucially on details of the SIP initialisation and various characteristics of the initialised SIP ensemble (an issue that is inherently absent in spectral bin models and has not been paid much attention in previous LCM studies).

The Remapping Algorithm (based on ideas of Andrejczuk et al., 2010) showed a poor performance, either no realistic rain mode developed or the solutions became unstable. The evaluation exercises presented in Andrejczuk et al. (2010) were not suited to reveal the obvious shortcomings or downplayed its severity. Based on our extensive tests, the algorithm cannot be recommended for further LCM applications, unless the stability issue is solved.

The Average Impact (AIM) algorithm (based on ideas of Riechelmann et al., 2012) can produce very good results, however, appears to be inflexible inasmuch as only the initially largest SIPs are allowed to grow in radius space. The performance depends on details of the SIP initialisation much more than, e.g. on the time step or the SIP number.

The probabilistic All-or-Nothing (AON) algorithm (based on ideas of Shima et al., 2009; Sölch and Kärcher, 2010) yields the best results and is the only algorithm that can cope with all tested kernels. Unlike to AIM, in AON it is not pre-determined which SIPs will eventually contribute to the large droplet mode. By design, any SIP can become significant at some point and the algorithm can cope with SIP initialisations that guarantee a broad spectrum of weighting factors. If an equal weights initialisation is used tremendously many SIPs are necessary for AON convergence as reported by (Shima et al., 2009). Many current (multi-dimensional) applications of LCMs use such SIP ensembles with a narrow spectrum of weighting factors causing a poor performance of the collection/aggregation algorithms. This should be clearly avoided in order to have collection/aggregation algorithms to work properly and/or efficiently. The time step and the bin resolution κ (used in the singleSIP-init) have values similar to those used in traditional spectral-bin models and hence the computational efforts of both approaches for the collection/aggregation treatment are in the same range. The presented box

Geosci. Model Dev. Discuss., doi:10.5194/gmd-2016-271, 2016
Manuscript under review for journal Geosci. Model Dev.
Published: 28 November 2016

model simulations are a first step towards a rigourous evaluation of collection/aggregation algorithms in more complex LCM applications (multidimensional domain, full microphysics).

6 Code availability

The programming language IDL was used to perform the simulations and produce the plots. The source code can be obtained from the first author. Pseudo-code of the algorithms is given in the text.

7 Competing interests

The authors declare that they have no conflict of interest.

Acknowledgements. The DFG (German Science Foundation) partly funded the first author (contract number UN286/1-2) and the second author (RA617/27-1). We thank A. Bott for providing us with his fortran code, L.-P. Wang for simulation data, M. Andrejczuk, S. Shima and P. L'Ecuyer for discussions.

Geosci. Model Dev. Discuss., doi:10.5194/gmd-2016-271, 2016
Manuscript under review for journal Geosci. Model Dev.
Published: 28 November 2016

Geoscientific Model Development Discussions
Open Access
EGU

924 **References**

925 Albrecht, B. A.: Aerosols, cloud microphysics, and fractional cloudiness, Science, 245, 1227–1230, 1989.
926 Andrejczuk, M., Reisner, J. M., Henson, B., Dubey, M. K., and Jeffery, C. A.: The potential impacts of pollution
927 on a nondrizzling stratus deck: Does aerosol number matter more than type?, J. Geophys. Res., 113, D19 204,
928 doi:0.1029/2007JD009445, 2008.
929 Andrejczuk, M., Grabowski, W. W., Reisner, J., and Gadian, A.: Cloud-aerosol interactions for boundary layer
930 stratocumulus in the Lagrangian cloud model, J. Geophys. Res., 115, D22 214, doi:10.1029/2010JD014248,
931 2010.
932 Andrejczuk, M., Gadian, A., and Blyth, A.: Stratocumulus over SouthEast Pacific: Idealized 2D simulations
933 with the Lagrangian Cloud Model, ArXiv e-prints, 1211.0193v1 [physics.ao-ph], 2012.
934 Arabas, S. and Shima, S.-i.: Large-Eddy Simulations of Trade Wind Cumuli Using Particle-Based Micro-
935 physics with Monte Carlo Coalescence, J. Atmos. Sci., 70, 2768–2777, doi:10.1175/JAS-D-12-0295.1,
936 http://dx.doi.org/10.1175/JAS-D-12-0295.1, 2013.
937 Arabas, S., Jaruga, A., Pawlowska, H., and Grabowski, W. W.: libcloudph++ 1.0: a single-moment bulk, double-
938 moment bulk, and particle-based warm-rain microphysics library in C++, Geosci. Model Dev., 8, 1677–1707,
939 doi:10.5194/gmd-8-1677-2015, http://www.geosci-model-dev.net/8/1677/2015/, 2015.
940 Ayala, O., Rosa, B., and Wang, L.-P.: Effects of turbulence on the geometric collision rate
941 of sedimenting droplets. Part 2. Theory and parameterization, New Journal of Physics, 10,
942 doi:10.1088/1367-2630/10/7/075016, 2008.
943 Berry, E. X.: Cloud Droplet Growth by Collection, J. Atmos. Sci., 24, 688–701,
944 http://dx.doi.org/10.1175/1520-0469(1967)024<0688:CDGBC>2.0.CO;2, 1967.
945 Berry, E. X. and Reinhardt, R. L.: An Analysis of Cloud Drop Growth by Collection Part II. Single Initial
946 Distributions, J. Atmos. Sci., 31, 1825–1831, doi:10.1175/1520-0469(1974)031<1825:AAOCDG>2.0.CO;2,
947 http://dx.doi.org/10.1175/1520-0469(1974)031<1825:AAOCDG>2.0.CO;2, 1974.
948 Bott, A.: A Flux Method for the Numerical Solution of the Stochastic Collection Equation,
949 J. Atmos. Sci., 55, 2284–2293, doi:10.1175/1520-0469(1998)055<2284:AFMFTN>2.0.CO;2,
950 http://dx.doi.org/10.1175/1520-0469(1998)055<2284:AFMFTN>2.0.CO;2, 1998.
951 Chen, S., Bartello, P., Yau, M. K., Vaillancourt, P. A., and Zwijsen, K.: Cloud Droplet Collisions
952 in Turbulent Environment: Collision Statistics and Parameterization, J. Atmos. Sci., 73, 621–636,
953 doi:10.1175/JAS-D-15-0203.1, 2016.
954 Connolly, P. J., Emersic, C., and Field, P. R.: A laboratory investigation into the aggregation ef-
955 ficiency of small ice crystals, Atmos. Chem. Phys., 12, 2055–2076, doi:10.5194/acp-12-2055-2012,
956 http://www.atmos-chem-phys.net/12/2055/2012/, 2012.
957 DeVille, R., Riemer, N., and West, M.: Weighted Flow Algorithms (WFA) for stochastic particle coagulation,
958 J. Comput. Phys., 230, 8427–8451, doi:10.1016/j.jcp.2011.07.027, 2011.
959 Devroye, L.: Non-Uniform Random Variate Generation, Springer-Verlag, New York,
960 doi:10.1007/978-1-4613-8643-8, 1986.
961 Estivill-Castro, V. and Wood, D.: A Survey of Adaptive Sorting Algorithms, ACM Comput. Surv., 24, 441–476,
962 doi:10.1145/146370.146381, http://doi.acm.org/10.1145/146370.146381, 1992.

Geosci. Model Dev. Discuss., doi:10.5194/gmd-2016-271, 2016
Manuscript under review for journal Geosci. Model Dev.
Published: 28 November 2016

963 Gillespie, D. T.: The Stochastic Coalescence Model for Cloud Droplet Growth, J. At-
964 mos. Sci., 29, 1496–1510, doi:10.1175/1520-0469(1972)029<1496:TSCMFC>2.0.CO;2,
965 http://dx.doi.org/10.1175/1520-0469(1972)029<1496:TSCMFC>2.0.CO;2, 1972.
966 Golovin, A. M.: The solution of the coagulation equation for cloud droplets in a rising air current, Bull. Acad.
967 Sci. USSR, Geophys. Ser., 5, 783–791, 1963.
968 Grabowski, W. W. and Wang, L.-P.: Growth of Cloud Droplets in a Turbulent Environment,
969 Annual Review of Fluid Mechanics, 45, 293–324, doi:10.1146/annurev-fluid-011212-140750,
970 http://dx.doi.org/10.1146/annurev-fluid-011212-140750, 2013.
971 Hall, W. D.: A Detailed Microphysical Model Within a Two-Dimensional Dy-
972 namic Framework: Model Description and Preliminary Results, J. Atmos.
973 Sci., 37, 2486–2507, doi:10.1175/1520-0469(1980)037<2486:ADMMWA>2.0.CO;2,
974 http://dx.doi.org/10.1175/1520-0469(1980)037<2486:ADMMWA>2.0.CO;2, 1980.
975 Heymsfield, A. and Westbrook, C.: Advances in the estimation of ice particle fall speeds using laboratory and
976 field measurements, J. Atmos. Sci., 67, 2469–2482, 2010.
977 Hoffmann, F.: The Effect of Spurious Cloud Edge Supersaturations in Lagrangian Cloud Models: An Analytical
978 and Numerical Study, Mon. Weather Rev., 144, 107–118, doi:10.1175/MWR-D-15-0234.1, 2016.
979 Hoffmann, F., Raasch, S., and Noh, Y.: Entrainment of aerosols and their activation in a shal-
980 low cumulus cloud studied with a coupled LCM-LES approach, Atmos. Res., 156, 43 – 57,
981 doi:http://dx.doi.org/10.1016/j.atmosres.2014.12.008, 2015.
982 Kessler, E.: On distribution and continuity of water substance in atmospheric circulations, Mon. Americal Met.
983 Soc., Boston, 10, 1–84, 1969.
984 Khain, A., Ovtchinnikov, M., Pinsky, M., Pokrovsky, A., and Krugliak, H.: Notes on the state-of-the-art numer-
985 ical modeling of cloud microphysics, Atmos. Res., 55, 159–224, 2000.
986 Khairoutdinov, M. and Kogan, Y.: A new cloud physics parameterization in a large-eddy simulation model of
987 marine stratocumulus, Mon. Wea. Rev., 128, 229–243, 2000.
988 Kolodko, A. and Sabelfeld, K.: Stochastic particle methods for Smoluchowski coagulation equation:
989 Variance reduction and error estimations, Monte Carlo Methods and Applications, 9, 315–339,
990 doi:10.1163/156939603322601950, 2003.
991 Kostinski, A. and Shaw, R.: Fluctuations and luck in droplet growth by coalescence, Bull. Am. Meteorol. Soc.,
992 86, 235–244, doi:10.1175/BAMS-86-2-235, 2005.
993 L'Ecuyer, P. and Simard, R.: TestU01: A C Library for Empirical Testing of Random Number Generators, ACM
994 Trans. Math. Softw., 33, doi:10.1145/1268776.1268777, http://doi.acm.org/10.1145/1268776.1268777,
995 2007.
996 Lee, J., Noh, Y., Raasch, S., Riechelmann, T., and Wang, L.-P.: Investigation of droplet dynamics in a
997 convective cloud using a Lagrangian cloud model, Meteorology and Atmospheric Physics, 124, 1–21,
998 doi:10.1007/s00703-014-0311-y, cited By 0, 2014.
999 Long, A. B.: Solutions to the Droplet Collection Equation for Polynomial Kernels, J. At-
1000 mos. Sci., 31, 1040–1052, doi:10.1175/1520-0469(1974)031<1040:STTDCE>2.0.CO;2,
1001 http://dx.doi.org/10.1175/1520-0469(1974)031<1040:STTDCE>2.0.CO;2, 1974.

Geosci. Model Dev. Discuss., doi:10.5194/gmd-2016-271, 2016
Manuscript under review for journal Geosci. Model Dev.
Published: 28 November 2016

1002 Maisels, A., Einar Kruis, F., and Fissan, H.: Direct simulation Monte Carlo for simultaneous nucleation,
1003 coagulation, and surface growth in dispersed systems, Chemical Engineering Science, 59, 2231–2239,
1004 doi:10.1016/j.ces.2004.02.015, 2004.
1005 Maronga, B., Gryschka, M., Heinze, R., Hoffmann, F., Kanani-Sühring, F., Keck, M., Ketelsen, K., Letzel,
1006 M. O., Sühring, M., and Raasch, S.: The Parallelized Large-Eddy Simulation Model (PALM) version 4.0 for
1007 atmospheric and oceanic flows: model formulation, recent developments, and future perspectives, Geosci.
1008 Model Dev., 8, 2515–2551, doi:10.5194/gmd-8-2515-2015, http://www.geosci-model-dev.net/8/2515/2015/,
1009 2015.
1010 Matsumoto, M. and Nishimura, T.: Mersenne Twister: a 623-dimensionally equidistributed uniform pseudo-
1011 random number generator, ACM Transactions on Modeling and Computer Simulation, 8, 3–30, 1998.
1012 Mitchell, D.: Use of mass- and area-dimensional power laws for determining precipitation particle terminal
1013 velocities, J. Atmos. Sci., 53, 12, 1710 – 1723, 1996.
1014 Naumann, A. K. and Seifert, A.: A Lagrangian drop model to study warm rain microphysical processes in
1015 shallow cumulus, J. Adv. Model. Earth Syst., 7, 1136–1154, 2015.
1016 Paoli, R., Hélie, J., and Poinsot, T.: Contrail formation in aircraft wakes, J. Fluid Mech., 502, 361–373, 2004.
1017 Paoli, R., Nybelen, L., Picot, J., and Cariolle, D.: Effects of jet/vortex interaction on contrail formation in
1018 supersaturated conditions, Phys. Fluids, 25, 1–28, 2013.
1019 Rade, L. and Westergren, B.: Springers mathematische Formeln: Taschenbuch für Ingenieure,
1020 Naturwissenschaftler, Informatiker, Wirtschaftswissenschaftler, Springer Berlin Heidelberg,
1021 doi:10.1007/978-3-642-57239-5, 2000.
1022 Riechelmann, T., Noh, Y., and Raasch, S.: A new method for large-eddy simulations of clouds with Lagrangian
1023 droplets including the effects of turbulent collision, New Journal of Physics, 14, 065 008, 2012.
1024 Riemer, N., West, M., Zaveri, R. A., and Easter, R. C.: Simulating the evolution of soot mixing state with a
1025 particle-resolved aerosol model, J. Geophys. Res., 114, n/a–n/a, doi:10.1029/2008JD011073, d09202, 2009.
1026 Schmitt, C. G. and Heymsfield, A. J.: The Dimensional Characteristics of Ice Crystal Ag-
1027 gregates from Fractal Geometry, J. Atmos. Sci., 67, 1605–1616, doi:10.1175/2009JAS3187.1,
1028 http://dx.doi.org/10.1175/2009JAS3187.1, 2010.
1029 Scott, W. T.: Analytic Studies of Cloud Droplet Coalescence I, J. At-
1030 mos. Sci., 25, 54–65, doi:10.1175/1520-0469(1968)025<0054:ASOCDC>2.0.CO;2,
1031 http://dx.doi.org/10.1175/1520-0469(1968)025<0054:ASOCDC>2.0.CO;2, 1968.
1032 Seifert, A. and Beheng, K. D.: A double-moment parameterization for simulating autoconversion, accretion and
1033 selfcollection, Atmos. Res., 59, 265–281, 2001.
1034 Shima, S., Kusano, K., Kawano, A., Sugiyama, T., and Kawahara, S.: The super-droplet method for the numer-
1035 ical simulation of clouds and precipitation: a particle-based and probabilistic microphysics model coupled
1036 with a non-hydrostatic model, Q. J. R. Meteorol. Soc., 135, 1307–1320, 2009.
1037 Shirgaonkar, A. and Lele, S.: Large Eddy Simulation of Early Stage Contrails: Effect of Atmospheric Properties,
1038 44 th AIAA Aerospace Sciences Meeting and Exhibit, 0, 1–13, 2006.
1039 Simmel, M., Trautmann, T., and Tetzlaff, G.: Numerical solution of the stochastic collection equation - com-
1040 parison of the Linear Discrete Method with other methods, Atmos. Res., 61, 135–148, 2002.

Geosci. Model Dev. Discuss., doi:10.5194/gmd-2016-271, 2016
Manuscript under review for journal Geosci. Model Dev.
Published: 28 November 2016

1041 Sölch, I. and Kärcher, B.: A large-eddy model for cirrus clouds with explicit aerosol and ice microphysics and
1042 Lagrangian ice particle tracking, Q. J. R. Meteorol. Soc., 136, 2074–2093, 2010.
1043 Sölch, I. and Kärcher, B.: Process-oriented large-eddy simulations of a midlatitude cirrus cloud system based
1044 on observations, Q. J. R. Meteorol. Soc., 137, 374–393, 2011.
1045 Tzivion, S., Feingold, G., and Levin, Z.: An Efficient Numerical Solution to the Stochastic Collection
1046 Equation, J. Atmos. Sci., 44, 3139–3149, doi:10.1175/1520-0469(1987)044<3139:AENSTT>2.0.CO;2,
1047 http://dx.doi.org/10.1175/1520-0469(1987)044<3139:AENSTT>2.0.CO;2, 1987.
1048 Unterstrasser, S.: Large eddy simulation study of contrail microphysics and geometry during the vor-
1049 tex phase and consequences on contrail-to-cirrus transition, J. Geophys. Res., 119, 7537–7555,
1050 doi:10.1002/2013JD021418, http://dx.doi.org/10.1002/2013JD021418, 2014.
1051 Unterstrasser, S. and Görsch, N.: Aircraft-type dependency of contrail evolution, J. Geophys. Res., 119, 14,015–
1052 14,027, doi:10.1002/2014JD022642, http://dx.doi.org/10.1002/2014JD022642, 2014JD022642, 2014.
1053 Unterstrasser, S. and Sölch, I.: Optimisation of simulation particle number in a Lagrangian
1054 ice microphysical model, Geosci. Model Dev., 7, 695–709, doi:10.5194/gmd-7-695-2014,
1055 http://www.geosci-model-dev.net/7/695/2014/, 2014.
1056 Unterstrasser, S., Gierens, K., Sölch, I., and Wirth, M.: Numerical simulations of homogeneously nucleated nat-
1057 ural cirrus and contrail-cirrus. Part 2: Interaction on local scale, Meteorol. Z., doi:10.1127/metz/2016/0780,
1058 http://dx.doi.org/10.1127/metz/2016/0780, 2016.
1059 Wang, L.-P., Xue, Y., Ayala, O., and Grabowski, W. W.: Effects of stochastic coalescence and air turbulence on
1060 the size distribution of cloud droplets, Atmos. Res., 82, 416–432, 2006.
1061 Wang, L.-P., Xue, Y., and Grabowski, W. W.: A bin integral method for solving the kinetic collection equation,
1062 J. Comput. Phys., 226, 59–88, 2007.
1063 Xue, H., Feingold, G., and Stevens, B.: Aerosol effects on clouds, precipitation, and the organization of shallow
1064 cumulus convection, J. Atmos. Sci., 65, 392–406, 2008.